# Development and application of a method for imaging interstitial iron distribution in multicrystalline silicon wafers

*by*

Ole-Aleksander Haram Olsen


*Thesis submitted for the degree of*
MASTER OF SCIENCE
Faculty of Mathematics and Natural Sciences

UNIVERSITETET I OSLO

December 2014

2014

Development and application of a method for imaging Fe distribution in multicrystalline silicon wafers

Ole-Aleksander Haram Olsen

http://www.duo.uio.no/

Trykk: Reprosentralen, Universitetet i Oslo

# Abstract

**A new procedure for iron-mapping using photoluminescence imaging is proposed that enables use of the technique for a wider range of wafers and enables an easy and transparent evaluation of the obtained data. The effects temperature, FeB association and surface layer degradation have upon the measurements are evaluated. Using the new procedure the lateral and vertical Fe concentration through a mc-Si block is investigated. It is found that the Fe concentration increases rapidly in the middle section of the block. An analysis leads to the conclusion that this rapid increase is related to an increase in dislocation clusters.**

# Preface and acknowledgements

This thesis was written as part of the master program Materials, Energy and Nanotechnology at the University of Oslo. The work was performed at “Institutt for energiteknikk” (IFE) at Kjeller, Norway.

The amount of Fe in mc-Si wafers has steadily been decreasing over time as new and improved production techniques have been developed. The Fe concentration has fallen below the detection limit of many techniques previously used for analysis. Due to Fe being very electrically active, techniques based on lifetime spectroscopy enable detection of low Fe concentrations. A technique developed for imaging Fe using photoluminescence has proven to be very sensitive and can detect very low Fe concentrations. This work was motivated by the need for imaging techniques to be able to detect these diminished concentrations as they are still restricting the minority carrier lifetime (or lifetime for short). The field of defect characterization is to a large degree dependent upon the available measurement techniques.

I would like to thank IFE for the opportunity to conduct the research for my master thesis there, I am very grateful for the opportunity given to me. A special thanks goes to my supervisor, Dr. Erik Stensrud Marstein, for his support and guidance during this time. I would also like to thank Dr. Rune Søndenå and M.Sc. Marie Syre Wiig for providing me with valuable insight and fruitful academic discussions. A warm thank you goes out to the rest of the research group at the solar department and IFE for being helpful and supportive, and giving me a pleasant work environment. I would also like to thank REC for providing the wafers that were crucial to this work.

Lastly I would like to thank my family for all their support through this period of hard work. Their guidance and motivation have been of the utmost importance.

# Table of contents

Includes 23 figures and 5 tables

# Chapter 1: Introduction and background

## Section 1.1: Introduction

While the energy consumption of the world keeps growing at an alarming rate, the cost of energy produced by a solar panel is decreasing rapidly. While carbon based energy sources are finite, solar energy is, for all intents and purposes, infinite. While there are other green resources to be taken advantage of, such as wind, thermal and nuclear, solar is one of the top candidates to become the main energy production method. Solar energy is clean, safe, and, in large parts of the world, economically feasible. Cost, however, remains an obstacle in many regions. The goal of grid parity, a measure of the competitiveness of solar electricity to the local electricity cost, had been reached in 2013 in several countries, including Germany, Italy, Spain and Denmark [1]. The decreased cost of photovoltaic power is fuelling a massive expansion of solar power production. According to a recent report by the European Photovoltaic Industry Association, in 2013 the worldwide capacity installation followed the trend of this millennium; an exponential increase [2]. Worldwide installation came to more than 38GW [2].

Insolation values in most of Norway, to a certain extent prohibit the large scale installation seen in other European countries. Due to other green energy systems covering the electricity need in this country, the need for solar power is also lower. Norway does, however, have a prominent position in solar technology development and production. This is in large part due to having readily available green energy for use in silicon production, as well as having a competent workforce within material technology research.

Advances in other fields, such as battery capacity and cost, is making small personal solar power production systems more desirable, both on- and off-grid. At the same time, the lower cost of modules is enabling plants with higher output, further decreasing costs. Due to the decreased fraction of the cost of a system coming from the solar cells themselves, high-efficiency cells are becoming more and more valuable. As such, the development of new characterization methods becomes more important both for research and for production quality control. One of the parameters greatly influencing the efficiency of solar cells is the minority carrier lifetime (or lifetime for short), defined as the average time a charge carrier spends in an excited state before recombining. This value is determined by the underlying defect structure of a wafer. This underlying defect structure is important both for research purposes and industry production control and development. Being such an important issue, having access to better tools for use in defect characterization is therefore important for the continued development of solar cells.

Silicon (Si) is by far the most widely used material for commercial solar cells. Silicon is among the most abundant materials on earth, and many methods exist to extract highly purified silicon.

The most common Si material used in solar cell manufacturing is multicrystalline silicon (mc-Si).

Iron (Fe) is introduced into wafers during processing and is one of the most recombination active defects. As such, it is often the lifetime-limiting defect in mc-Si wafers. Both the effects of the Fe concentration and the Fe distribution have been discussed in literature. The distribution of Fe in mc-Si wafers affects both the lifetime distribution and the average lifetime. For instance, the average lifetime can be increased significantly by gettering. This is attributed to thermal relocation of Fe (and other impurities) into grain boundaries and other regions of high defect concentrations. Due to distribution of Fe having a large impact on the efficiency of finished cells, it is of great interest to evaluate the evolution of Fe distribution throughout a Si block. Several effective methods for obtaining Fe distribution maps have been developed, many of which are based on a principle reported by Zoth and Bergholz [3]. They reported that a difference in lifetime before and after light-soaking of wafers with a recombination activity dominated by Fe can be used to measure the Fe concentration. Based on this principle, MacDonald, Tan, and Trupke developed a method for imaging Fe distribution by use of photoluminescence (PL) imaging [4]. The technique presented enabled quick and fairly accurate measurement of iron distribution in wafers.

## Section 1.2: Purpose of this work

The efficiency of a solar cell is directly related to the lifetime of charge carriers. As previously mentioned, Fe is often the lifetime limiting defect. Developing techniques to quickly acquire an image of the Fe concentration across a wafer can lead to a better understanding of the mechanisms causing Fe to be incorporated during crystal growth. An understanding of the underlying mechanism may in turn lead to better production methods.

In conjunction with better production methods, the amount of point defects such as Fe is diminishing. Due to Fe still being the cause of low lifetime in many wafers, imaging techniques that allow for measurement of its concentration are needed.

The goal of this thesis was to investigate the Fe distribution through a Si block using the PL imaging technique. Due to the complexity of defect-dominated recombination and a large variation between samples, the existing technique proved insufficient for characterization of our wafers. As such, a more transparent procedure that made it easier to evaluate sources of unexpected results had to be developed, before the investigation of the Fe distribution in the block could commence. The main obstacle of using PL imaging for obtaining Fe distribution maps is a complex excess carrier density dependent lifetime that is dependent, among other things, upon the surface passivation layer, the temperature of the wafer, and the light-affected

chemical state of iron, oxygen, and copper. In order to examine the validity of the presented procedure, it is necessary to limit the impact of all light-affected parameters other than Fe.

The procedure was then used to obtain Fe images of select wafers throughout a single Si block to investigate Fe distribution trends.

The structure of this thesis is as follows:

Chapter 2 introduces background theory as well as what others have done before that is relevant to the present work. The main goal of the chapter is to present the reader with a thorough understanding of Shockley-Read-Hall (SRH) recombination; the basis of lifetime spectroscopy (the use of lifetime for defect characterization). The operating principles of the measurement techniques used in this work are also presented here.

Chapter 3 discusses experimental details, including wafer parameters and their measurement. In addition, this chapter introduces the modified procedure for measurement of the spatial variation of Fe. Chapter 4 presents the results of measurement and simulation to prove the validity and accuracy of the new procedure. Additionally, chapter 4 contains the results of measurements on all wafers, and, by necessity, some discussion of the obtained results.

Chapter 5 contains an extended discussion of error sources, the validity of the procedure, and an examination of the obtained results. Chapter 6 finalizes the thesis by concluding remarks.

# Chapter 2: General theory

## Section 2.1: An overview of chapter contents

In order to discuss the Fe distribution imaging technique it is necessary to have an understanding of the complex SRH recombination theory, light-induced degradation effects, and the measurement techniques. Section 2.1.2 details the principle of solar cell operation. Section 2.2 presents generally accepted theory of light induced degradation (LID) effects. In section 2.3, the mechanism of recombination through defect states is derived. Section 2.4 deals with the main measurement techniques utilized in this work.

### Section 2.1.2: Solar cell principle of operation

Solar cells operate on the principle of the photovoltaic effect, defined by the Encyclopædia Britannica as; "[a] process in which two dissimilar materials in close contact produce an electrical voltage when struck by light or other radiant energy."

When a p-type and an n-type material are in intimate contact, the free electrons from the n-side diffuse to the p-side and vice versa for holes, due to the large gradient in carrier density. This diffusion current causes ionized dopants on either side of the contact to be exposed. These stationary charges set up an electric field that opposes the movement of charge carriers across the contact area. Figure 1 depicts the steady-state condition. In equilibrium, the drift and diffusion currents cancel each other out, resulting in no net transport of charge carriers. Under illumination, charge carriers are created that can contribute to a current.

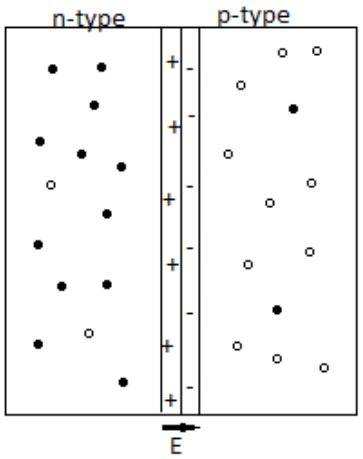


**Figure 1: A depiction an n-type and a p-type material in intimate contact. Filled circles represent electrons while empty circles represent holes.**

When the two materials are connected by a low-resistance external circuit, charge carriers will drift from one and into the other material. Power can be extracted in accordance with the relation $P = IV$, where $I$ is the current and $V$ is the voltage. A typical current-voltage relationship for a solar cell is depicted in figure 2.

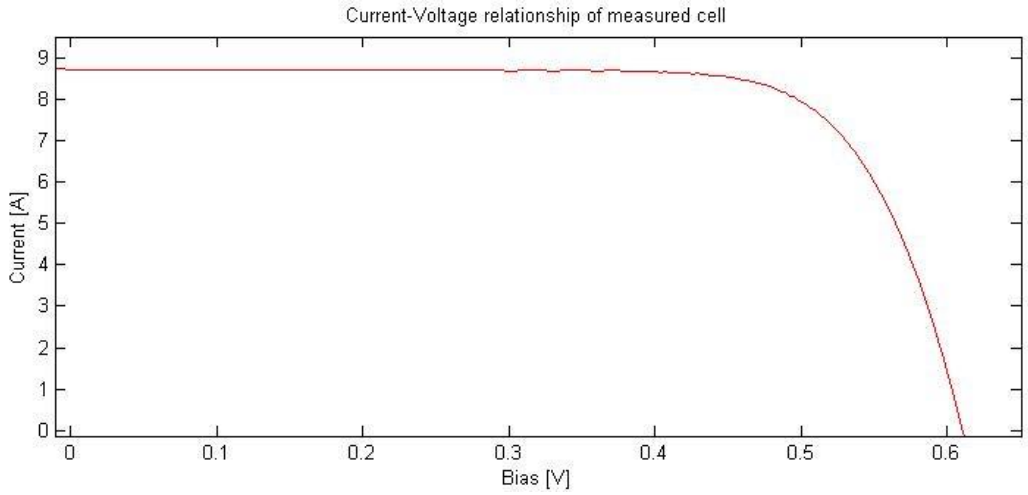


**Figure 2: A typical IV-relationship of a solar cell.**

For a deeper understanding of the principle of solar cell operation, readers can refer to any standard text-book on solar cells, for instance: "The Physics of Solar Cells", by Jenny Nelson.

## Section 2.2: Overview of light-induced degradation (LID)

### Section 2.2.1: Light-induced degradation of iron-boron complexes

The main physical principle utilized in Fe imaging is the light-induced degradation of iron-boron complexes (Fe-LID). Fe is present in many mc-Si wafers due to contamination during production. The equilibrium reaction equation of the point defect is given as $Fe_i^+ + B^- \rightleftharpoons FeB$ [3]. In darkness, Fe and B tend to associate and form FeB complexes. However, this reaction is driven towards the left by illumination. Interstitial Fe ($Fe_i$) is more recombination active than FeB at illumination levels at and below 1 sun (approximately 1000 $W/m^2$). At illumination levels significantly above 1 sun, the shallow recombination center FeB is the most recombination active. The difference in the injection dependent minority carrier lifetime of the two point-defects results in a crossover of the injection dependent lifetime curves. If Fe-LID is the only LID mechanism in the sample, the crossover point (defined as the excess minority carrier density at which the injection dependent lifetime curves cross) can be used as an identifier of $Fe_i$ presence [5].

The proportion of iron present as FeB before dissociation by illumination and the proportion of interstitial iron after dissociation have been discussed in literature[6]. It was there determined

that resting a sample in the dark at room temperature for 12h ensures almost complete repairing (more than 99%) for a sample with a boron dopant density of $1*10^{16}$ $cm^{-3}$. Samples used in this work rarely had doping levels significantly below this value, which ensures fast repairing. Nonetheless, all samples were allowed to rest in darkness for a minimum of 24 hours before measurement.

To ensure that the fraction of Fe present as interstitial Fe after dissociation is close to unity, several papers suggest specific illumination times [4][6]. In this work, it was found that the dissociation saturates earlier than previously expected.

### Section 2.2.2: Other light-induced degradation (LID) effects

Boron-oxygen (BO) is a meta-stable complex, formed in boron-doped Si wafers/cells under illumination, which can cause a severely reduced minority carrier lifetime and solar cell efficiency under operation. The complex is stable at room temperature. The LID can be reversed and complete dissociation can be achieved by annealing at $200^0$C for 10 minutes [7][8].

The illumination time necessary to achieve complete degradation varies depending on the boron doping level [8]. For doping levels close to $1*10^{16}$ $cm^{-3}$, complete degradation was in this work assumed after illumination by 1 sun for 24 hours. Some wafers were instead exposed to light from fluorescent tubes for 96 hours. The rated luminosity of the tubes causes an excess carrier density well above the reported excess carrier density at which the rate of BO complex generation saturates [9].

A possible light-induced degradation of the passivation layer was observed in this work. This degradation causes an excess carrier density dependent decrease in the effective lifetime, where the effect is strongest at higher excess carrier densities. It was found that the surface LID became much more pronounced if strong illumination was utilized. Additionally, this degradation was found to be dependent upon the illumination time, where the degradation was decreased substantially (to the point where it was no longer possible to observe it in QSSPC measurements) if short illumination times were used. It must be pointed out that this LID effect has not been unambiguously proven in this work. It may be that some unidentified defect is the cause. Section 4.4.2 provides an overview of the experimentally observed effect that provides an indication of the passivation layer being the cause.

Copper (Cu) is another defect that can cause LID. It has been proposed that illumination enables precipitation of Cu in the wafer bulk [10]. They reported finding that LID caused by Cu behaves in a similar manner to that of BO-LID. Separation of the two LID effects is therefore difficult without special wafer preparation, and as such has not been included in this work. It was in this work assumed that the concentration of Cu was low enough that Fe-LID would dominate the minority carrier lifetime and the effect of Cu therefore would be negligible.

## Section 2.3: Recombination

In any material with a temperature above absolute zero, some electrons escape their atom and are free to move within the structure. In addition, holes are generated at the atomic site, which are also free to move. The rate at which carriers are generated depend upon both external factors (such as illumination) and internal factors (having a finite temperature). At thermal equilibrium, there must exist a process which is equal and opposite to that of the generation rate. This recombination rate is caused by electrons and holes annihilating each other. For instance, an electron may relax back into an unoccupied atomic energy level, thereby decreasing the amount of free carriers.

Recombination is caused by several factors, both intrinsic (caused by fundamental material properties) and extrinsic (caused by other factors, such as the existence of foreign atoms) in nature. The most important recombination pathways are Auger recombination, radiative recombination, and Shockley-Read-Hall (SRH) recombination. Auger recombination and radiative recombination are intrinsic recombination mechanisms, while SRH recombination is extrinsic. Auger recombination is generally viewed as a three particle process in which one carrier relaxes across the band gap and recombines, while giving its excess energy off to a third particle. Radiative recombination is caused by a charge carrier relaxing across the band gap while giving off its energy as photons. The intrinsic recombination pathways are illustrated in figure 3.

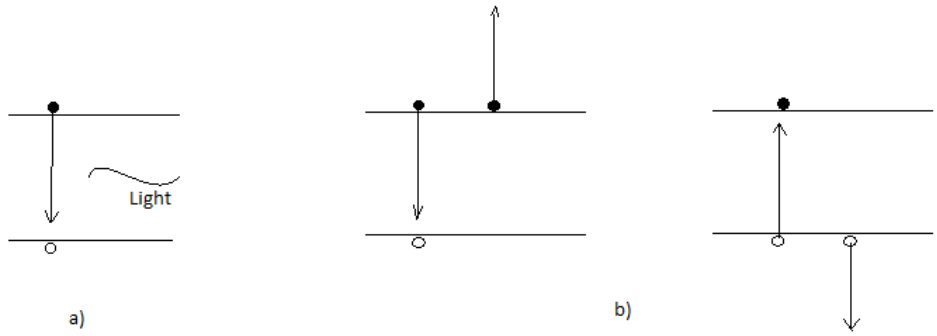


**Figure 3: Intrinsic recombination mechanisms. a) Radiative recombination, b) Auger recombination**

In order for a charge carrier generated by light to contribute to the current of a solar cell, it must survive until being collected by an external circuit. The recombination rate therefore directly influences the current generated, and so by extension, the efficiency of the cell.

### Section 2.3.1: Theory of Shockley-Read-Hall recombination

In order to analyze defect specific recombination paths it is necessary to have a good understanding of Shockley-Read-Hall (SRH) recombination. This section focuses on the basic

derivation of the SRH recombination mechanism. Section 2.3.2 investigates the effect of temperature on SRH lifetime. Section 2.3.3 discusses the crossover point. Section 2.3.4 addresses the use of SRH theory to determine the interstitial Fe concentration (hereafter Fe concentration) from lifetime images.

Extrinsic recombination is often the dominant recombination mechanism at low excess carrier densities (low injection level) in indirect band gap materials. During production of mc-Si wafers, many contaminants are introduced unintentionally by processing tools and raw materials. Defects in the Si crystal structure may induce states in the band gap. The discrete energy levels of the states are determined by the defect in question. Deep defect levels (close to the center of the band gap) tend to be pathways for recombination, while shallow defect levels (close to one of the band edges) tend to only temporarily trap carriers from the band closest to it.

Charge carriers can interact with a trap/recombination center in many different ways. An empty trap level (occupied by a hole), may capture an electron from either the conduction band or the valence band. A filled trap (occupied by an electron), may emit an electron into either the conduction band or the valence band. In addition, there are equivalent processes for holes. As a hole is simply the absence of an electron, many of these processes are equivalent. Recombination can be regarded in four ways, all of which are in essence equivalent. These processes are depicted in figure 4.

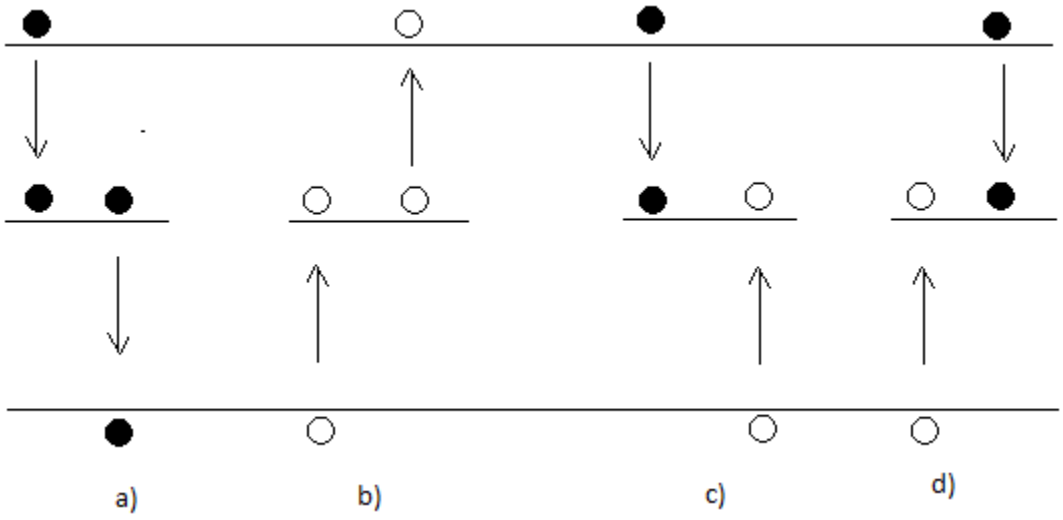


**Figure 4: Representation of how recombination occurs due to the interaction of carriers with traps. a) represents an electron relaxing to the valence band via a trap level. b) represents a hole being captured by a trap and subsequently being emitted to the conduction band. . c) is the equivalent of a) where the process is represented instead by capture of a hole from the valence band. d) is a process equivalent of process b), instead represented by an electron capture.**

An electron may be captured from the conduction band and subsequently being emitted to the valence band. A hole may be captured from the valence band and subsequently be emitted to the conduction band. An electron/hole may be captured by a trap which subsequently captures a hole/electron. All these processes are equivalent, except for the order in which carriers are captured/emitted.

The theory developed by Shockley, Read and Hall regards the recombination rate through a single defect energy level.

In order to determine the rate of recombination through defects it is instructive to address capture and emission rates first. The rate at which a carrier is captured by a single trap is dependent upon the density of carriers, the capture cross-section of the trap, and the thermal velocity of the carrier:

$$\boldsymbol{C_e = v_{th}\sigma_n n} \qquad \textbf{2-1}$$

$$\boldsymbol{C_h = v_{th}\sigma_p p} \qquad \textbf{2-2}$$

where $C_{e\backslash h}$ are the capture rates of electrons or holes, $v_{th}$ is the thermal velocity, $\sigma_{n\backslash p}$ are the capture crossections and n/p are the free carrier concentrations. The capture cross-section is defined as the area around the point defect in which a charge carrier will have a high probability (100% probability for the purpose of calculations) of being captured by it. For a collection of defects the complete capture rate is:

$$\boldsymbol{C_e^{tot} = v_{th}\sigma_n n N_t(1 - f_t)} \qquad \textbf{2-3}$$

$$\boldsymbol{C_h^{tot} = v_{th}\sigma_p p N_t(f_t)} \qquad \textbf{2-4}$$

where $N_t$ is the density of traps and $f_t$ is the fraction of traps occupied by electrons.

The emission rates are unknown, but can be calculated for the case of thermal equilibrium due to the requirement that the time rate of change of the carrier populations must equal zero ($\mathrm{dn/dt} = 0$). The derivation will be performed for electrons, but the mechanism for hole emission is the same:

$$\boldsymbol{\frac{dn}{dt} = E_e * N_t f_t - C_e^{tot}} \qquad \textbf{2-5}$$

which, together with equation 2-3 gives at thermal equilibrium:

$$\boldsymbol{E_e = \sigma_n v_{th} n \left(\frac{1 - f_t}{f_t}\right)} \qquad \textbf{2-6}$$

where $E_e$ is the emission rate. The equilibrium electron concentration, $n_0$, derived in any basic textbook on semiconductors, is given by:

$$\boldsymbol{n_0 = N_c e^{-\left(\frac{E_C - E_F}{k_B T}\right)}} \qquad \textbf{2-7}$$

where $N_c$ is the effective density of states in the conduction band, $E_F$ is the Fermi energy-level, $E_C$ is the conduction band energy level, $k_B$ is Boltzmann's constant and $T$ is the temperature in degrees Kelvin. The probability of occupation is given by the Fermi-Dirac distribution function:

$$\boldsymbol{f_t(E_t) = \left[1 + e^{\frac{E_t - E_F}{k_B T}}\right]^{-1}} \qquad \textbf{2-8}$$

where $E_t$ is the trap energy level. Inputting equations 2-7 and 2-8 into equation 2-6 returns an expression for the emission rate:

$$\boldsymbol{E_e = \sigma_n v_{th} N_c e^{-\frac{E_C - E_t}{k_B T}}} \qquad \textbf{2-9}$$

From which we define the SRH density, $n_1$, as:

$$\boldsymbol{n_1 = N_c e^{-\frac{E_C - E_t}{k_B T}}} \qquad \textbf{2-10}$$

Using equations 2-9 and 2-5 allows for a determination of $f_t$ for non-equilibrium steady state conditions by use of the condition that $\frac{dn}{dt} = \frac{dp}{dt}$. Note that this requires an expression for the emission rate and time dependence of the hole density, which, for sake of brevity, have not been derived here. Inserting $f_t(\sigma_p, \sigma_n, n, p, n_1, p_1)$ back into equation 2-5 yields the SRH recombination rate, $U$.

The lifetime is defined as:

$$\boldsymbol{\tau = \frac{\Delta n}{U}} \qquad \textbf{2-11}$$

where U is the net recombination rate, $\Delta n$ is the excess carrier density, and $\tau$ is the lifetime.

From equation 2-11, and from assuming that carrier trapping is low (i.e.. the defect states act as recombination centers) so that $\Delta n = \Delta p$, and by replacing the non-equilibrium carrier densities by $n = n_0 + \Delta n$ and $p = p_0 + \Delta p$, we obtain for the SRH lifetime:

$$\tau_{SRH} = \frac{\tau_{n0}(p_0 + p_1 + \Delta n) + \tau_{p0}(n_0 + n_1 + \Delta n)}{p_0 + n_0 + \Delta n} \quad \textbf{2-12}$$

Here, the capture cross-sections, thermal velocity and trap density have been replaced by the so-called capture time constants:

$$\tau_{p0} = \left[N_t \sigma_p v_{th}\right]^{-1} \quad and \quad \tau_{n0} = \left[N_t \sigma_n v_{th}\right]^{-1} \quad \textbf{2-13}$$

Equation 2-12 can be further simplified by relating the asymmetry of capture cross-sections to a symmetry factor:

$$k \equiv \frac{\tau_{p0}}{\tau_{n0}} \quad \textbf{2-14}$$

From equations 2-12 and 2-14, the SRH lifetime is:

$$\tau_{SRH} = \tau_{n0}\left[\left(\frac{p_0 + p_1 + \Delta n}{p_0 + n_0 + \Delta n}\right) + k\left(\frac{n_0 + n_1 + \Delta n}{p_0 + n_0 + \Delta n}\right)\right] \quad \textbf{2-15}$$

For the purposes of this work, equation 2-15 is of the utmost importance. The SRH lifetime is the basis for obtaining Fe maps discussed in section 2.3.4.

The above derivation closely follows that of Stefan Rein, in his book Lifetime Spectroscopy [11], modified somewhat to fit the purpose of this work. For a more complete derivation of the SRH lifetime, readers are referred to his work.

### Section 2.3.2 Effects of temperature on SRH lifetime

The SRH lifetime given in equation 2-15 is affected by temperature like so:

$$\tau_{SRH}(T) = \tau_{n0}(T)\left[\frac{p_0(T) + p_1(T) + \Delta n}{p_0(T) + n_0(T) + \Delta n} + k\left(\frac{n_0(T) + n_1(T) + \Delta n}{p_0(T) + n_0(T) + \Delta n}\right)\right] \quad \textbf{2-16}$$

where the SRH densities are dependent upon temperature, the minority time constant is dependent upon temperature through the density of states and the thermal velocity, and the equilibrium carrier concentrations are dependent upon temperature via the intrinsic carrier concentration, $n_i$. Several of the parameters of equation 2-16 are affected by the temperature dependence of the densities of states given below:

$$N_{c\backslash v}(T) = N\left(\frac{m^*_{e\backslash h}(T)}{m_0}\right)^{\frac{3}{2}} * \left(\frac{T}{300K}\right)^{\frac{3}{2}} \quad \text{2-17}$$

where N is a numerical factor equal to $2.5409 * 10^{19}\text{cm}^{-3}$,[12] $m^*_{e\backslash h}$ are the effective electron/hole masses in the conduction/valence band, and $m_0$ is the electron rest mass. Interested readers may refer to reference 11 for a thorough review of the temperature dependence of the densities of states. $m^*_e(T)$ is given below:

$$\frac{m^*_e(T)}{m_0} = 6^{\frac{2}{3}}\left[\left(C\left(\frac{E_{gap}(0)}{E_{gap}(T)}\right)\right)^2\left(\frac{m_l}{m_0}\right)\right]^{\frac{3}{2}} \quad \text{2-18}$$

where the parameters are given in table 1. The energy gap is modelled as[11]:

$$E_{gap}(T) = E_{gap}(0) - \frac{\alpha T^2}{T+\beta} \quad \text{2-19}$$

where the relevant parameters, also obtained from Rein, are shown in table 1. $m^*_h(T)$ is given below:

$$\frac{m^*_h(T)}{m_0} = \left(\frac{a + bT + cT^2 + dT^3 + eT^4}{1 + fT + gT^2 + hT^3 + iT^4}\right)^{\frac{2}{3}} \quad \text{2-20}$$

where the relevant parameters are again given in table 1.

**Table 1: Parameters used in equations 2-17 to 2-20**

| Parameter | Value |
|---|---|
| a | 0.443587 |
| b | $0.3609528*10^{-2}$ |
| c | $0.1173515*10^{-3}$ |
| d | $0.1263218*10^{-5}$ |
| e | $0.3025581*10^{-8}$ |
| f | $0.4683382*10^{-2}$ |
| g | $0.2286895*10^{-3}$ |
| h | $0.7469271*10^{-6}$ |
| i | $0.172748*10^{-8}$ |
| $E_{gap}(0)$ | 1.170eV |
| $\alpha$ | $4.73*10^{-4}$ eV/K |
| $\beta$ | 636K |
| C | 0.1905 |
| $m_l/m_0$ | 0.9163 |

The temperature dependence of the time constants is complex, but for the purposes of this work it is assumed that the symmetry factor is independent of temperature and that the capture cross section is independent in the relevant temperature range (300-320K). The full temperature dependency of the minority time constant is then:

$$\boldsymbol{\tau_{n0}(T) = \frac{1}{N_t * v_{th}^{300K} \left(\frac{T}{300K}\right)^{1\backslash 2} * \sigma_n}} \qquad \textbf{2-21}$$

Where $N_t$ is the trap density, $v_{th}^{300K} = 1.1 * 10^7 \mathrm{cm/s}$ (reference 5) and $\sigma_n$ is the minority carrier capture cross section.

The temperature dependence of the SRH densities are given by:

$$\boldsymbol{n_1(T) = N_C(T) e^{-\frac{E_C - E_t}{k_b T}}} \qquad \textbf{2-22}$$

$$\boldsymbol{p_1(T) = N_V(T) e^{-\frac{E_t - E_V}{k_b T}}} \qquad \textbf{2-23}$$

In order to discuss the validity of the assumptions and simplifications employed in the above derivation of the temperature dependency of the SRH lifetime, it is important to note that the temperature range investigated in this work was restricted to a small range around 300K. As no freeze-out of dopants or significant change to the intrinsic carrier concentration value can be expected in this range, any change to the equilibrium carrier concentrations has been neglected in the derivation. They are, however, included during simulations for increased accuracy. The temperature dependency of the capture cross-sections has been neglected due to their small temperature dependency around 300K, as discussed by Rein (reference 11).

### Section 2.3.3: Crossover point: An identifier of Fe

As previously discussed, FeB complexes are split under illumination. Using equation 2-15 it is possible to predict how this influences the lifetime. The electron capture time constant is simply a scaling factor of the lifetime, whose only parameter that changes in going from FeB to $Fe_i$ is the capture cross-section. The k-factor can be expected to change, influencing the shape of the $\tau(\Delta n)$ curve. The only other parameters that can be expected to change are those of the SRH densities. As FeB has a fairly shallow defect depth in the upper band gap half, while $Fe_i$ has a fairly deep defect depth in the lower band gap half, substantial changes to the injection dependent recombination activity can be expected. These changes to the high-level injection (HLI) lifetime, the low-level injection (LLI) lifetime, and the slope of the injection dependent

SRH lifetime cause $\tau_{SRH}^{Fe}(\Delta n)$ and $\tau_{SRH}^{FeB}(\Delta n)$ to cross each other. The excess minority carrier density at which they cross is defined as the crossover point.

From the definition of the crossover point we have that the crossover point will be found where:

$$\boldsymbol{\tau_{SRH}^{Fe} = \tau_{SRH}^{FeB}} \qquad \textbf{2-24}$$

What remains is to solve equation 2-24 for the excess carrier density, by using equation 2-15 for the SRH lifetime, under the assumption of p-type doping:

$$\boldsymbol{\tau_{n0}^{FeB}\left(\frac{p_1^{FeB}+p_0+\Delta n}{p_0+\Delta n}+k^{FeB}\left(\frac{n_1^{FeB}+\Delta n}{p_0+\Delta n}\right)\right) = \tau_{n0}^{Fe}\left(\frac{p_1^{Fe}+p_0+\Delta n}{p_0+\Delta n}+k^{FeB}\left(\frac{n_1^{Fe}+\Delta n}{p_0+\Delta n}\right)\right)} \qquad \textbf{2-25}$$

Dividing by the common denominator and collecting all excess carrier density terms on the left side we obtain:

$$\boldsymbol{\Delta n_x = \frac{\tau_{n0}^{Fe}\left(p_1^{Fe}+p_0+k^{Fe}n_1^{Fe}\right)-\tau_{n0}^{FeB}\left(p_1^{FeB}+p_0+k^{FeB}n_1^{FeB}\right)}{\left(\tau_{n0}^{FeB}(1+k^{FeB})-\tau_{n0}^{Fe}(1+k^{Fe})\right)}} \qquad \textbf{2-26}$$

where $\Delta n_x$ is the excess carrier density at which the crossover point is located. By further dividing both numerator and denominator by $\tau_{n0}^{FeB}$ it is possible to show that the crossover point is independent of the trap density. The crossover point was reported in literature to always be found in an excess carrier density range of 1.2 to 2e14cm$^{-3}$ for dopant densities below 5e16 cm$^{-3}$(ref 6). This was later corrected in reference 5, but the results therein (ref 5) do not match that of this work.

### Section 2.3.4: Fe concentration maps from lifetime images

As previously mentioned, it is possible to determine an Fe concentration due to the differing recombination activity of Fe and FeB. Their SRH lifetimes (for p-type material) are represented on the right and left side of equation 2-25. The minority carrier effective lifetime is given by:

$$\boldsymbol{\frac{1}{\tau} = \frac{1}{\tau_{SRH}} + \frac{1}{\tau_{aug}} + \frac{1}{\tau_{rest}}} \qquad \textbf{2-27}$$

where $\tau_{aug}$ is the lifetime due to Auger recombination, $\tau_{rest}$ is composed of all the other recombination pathways. Assuming that the rest of the recombination pathways have a very low injection dependency, subtracting the lifetime before splitting from that after splitting, returns, after some rearranging:

$$\frac{1}{\tau_{Fe}} - \frac{1}{\tau_{FeB}} = \frac{1}{\tau_1} - \frac{1}{\tau_0} - \frac{1}{\tau_{aug_1}} + \frac{1}{\tau_{aug_0}} \qquad \textbf{2-28}$$

Where the Auger lifetimes ($\tau_{aug_{1\backslash 0}}$) have been included due to the change in excess carrier density, and $\tau_{rest}$ has vanished due to the assumption mentioned above. The left side of equation 2-28 can be determined from equation 2-15. After some rearranging and extraction of the defect density we obtain:

$$N_t = \frac{1}{X^{Fe} - X^{FeB}} \left[\frac{1}{\tau_1} - \frac{1}{\tau_0} - \frac{1}{\tau_{aug_1}} + \frac{1}{\tau_{aug_0}}\right] \qquad \textbf{2-29}$$

where

$$X^{Fe} = \frac{v_{th}(N_A + \Delta n_{after})}{\left(\frac{1}{\sigma_p^{Fe}}\right)(n_1^{Fe} + \Delta n_{after}) + \left(\frac{1}{\sigma_n^{Fe}}\right)(N_A + p_1^{Fe} + \Delta n_{after})} \qquad \textbf{2-30}$$

$$X^{FeB} = \frac{v_{th}(N_A + \Delta n_{before})}{\left(\frac{1}{\sigma_p^{FeB}}\right)(n_1^{FeB} + \Delta n_{before}) + \left(\frac{1}{\sigma_n^{FeB}}\right)(N_A + p_1^{FeB} + \Delta n_{before})} \qquad \textbf{2-31}$$

A thorough discussion on the validity of this approach is given in reference 4. The Auger recombination rate can be modelled by[13]:

$$R_{auger} = np(1.8 * 10^{-24} n_0^{0.65} + 6 * 10^{-25} p_0^{0.65} + 3 * 10^{-27} \Delta n^{0.8}) \qquad \textbf{2-32}$$

A discussion of the validity and accuracy, in addition to a derivation of eq. 2-32 is contained within ref. 13. In this work, the authors obtained a good fit with experimental results for the entirety of the investigated injection range.

## Section 2.4: Measurement techniques

### Section 2.4.1: An overview

There exist quite a few measurement techniques able to estimate iron concentration in silicon wafers. Among these are deep-level transient spectroscopy (DLTS)[14], scanning surface-photovoltage (SPV)[15], and microwave-detected photoconductance decay ($\mu W - PCD$)[16]. For the purposes of this work, the techniques mainly used are Quasi-Steady State PhotoConductance (QSSPC) and photoluminescence imaging (PL). These techniques can be utilized to obtain an injection-level dependent lifetime and spatially resolved lifetime maps, respectively.

### Section 2.4.2: Quasi-steady-state Photoconductance

The QSSPC technique is used to measure minority carrier lifetime. The basis of the technique stems from the continuity equation of excess minority carriers (ref 11):

$$\frac{\delta \Delta n}{\delta t} = G_{bulk}(t,x) - U_{bulk}(t,x) + \frac{1}{q}\frac{dJ_n}{dx} \qquad \text{2-33}$$

where $\Delta n$ is the excess minority carrier density, $G_{bulk}$ is the photogeneration rate, $U_{bulk}$ is the recombination rate in the bulk and $J_n$ is the electron current density.

With uniform photogeneration over the sample and no surface recombination, the transport term of equation 2-33 vanishes. According to Rein, if there is surface recombination, this can be included in the recombination term for an effective recombination rate $U_{eff}$, which can be expressed as:

$$U_{eff} = \frac{\Delta n}{\tau_{eff}} \qquad \text{2-34}$$

using equation 2-33 and equation 2-34 one will arrive at:

$$\tau_{eff} = \frac{\Delta n}{G - \frac{\delta \Delta n}{\delta t}} \qquad \text{2-25}$$

for the effective lifetime. For quasi-steady state, here defined for when carrier lifetime is much smaller than the decay time of the generation source, this simplifies to:

$$\boldsymbol{\tau_{eff} = \frac{\Delta n}{G}} \qquad \textbf{2-36}$$

The QSSPC technique measures the excess carrier density (area averaged) by inductively measuring the photoconductance, $\Delta\boldsymbol{\sigma}$, given by:

$$\boldsymbol{\Delta\sigma = q * d * (\Delta n * \mu_n + \Delta p * \mu_p)} \qquad \textbf{2-37}$$

where $\boldsymbol{q}$ is the elementary charge, $\boldsymbol{d}$ is the sample thickness and $\boldsymbol{\mu_n}$ and $\boldsymbol{\mu_p}$ are the electron and hole mobilities, respectively. Assuming $\Delta n = \Delta p$ [17],

$$\boldsymbol{\Delta n = \frac{\Delta\sigma}{q * d * (\mu_n + \mu_p)}} \qquad \textbf{2-38}$$

which allows for the determination of the average excess carrier density in the area above the inductively coupled coil. The assumption of equal minority and majority excess carrier densities may fail in the presence of traps [18]. Due to minority carrier trapping, an excess amount of majority carriers are generated in order to obtain equilibrium, resulting in an overestimation of the excess photoconductance. Consequently, the minority carrier density and lifetime are overestimated in accordance with equations 2-36 and 2-38.

The generation rate in our setup from BTimaging is obtained from:

$$\boldsymbol{G = I_{inc,laser}(t) * \frac{1}{d} * (1 - R_{laser})} \qquad \textbf{2-39}$$

where $\boldsymbol{d}$ is the thickness of the sample and $\boldsymbol{R_{laser}}$ is the reflectivity of the sample at the wavelength of the incident laser light (808nm). $I_{inc,laser}(t)$ is the time-dependent monochromatic incident photon flux which is determined from a reference cell. It is further assumed that all incident light that is not reflected is absorbed, which holds for any mc-Si wafer of a thickness comparable to those used in this work when the photon energy is high.

Measuring the minority carrier lifetime inductively in conjunction with the generation rate then allows for a calculation of an injection dependent lifetime curve from equation 2-36.

### Section 2.4.3: Trapping

Minority carrier trapping is caused by defects trapping a carrier and subsequently releasing it to the band from where it came. This was briefly discussed in section 2.4.2. Some methods have been developed that correct for trapping (Macdonald, Sinton and Cuevas (2001)). An attempt was made during the course of this work to replicate the method. It was found that our method was unreliable and that it was difficult to ascertain the accuracy of it. As such, trapping correction was not performed.

### Section 2.4.4: Photoluminescence imaging

Photoluminescence (PL) imaging is a technique that utilizes radiative recombination in wafers and cells to provide a two-dimensional lifetime image. Figure 5 depicts the setup.

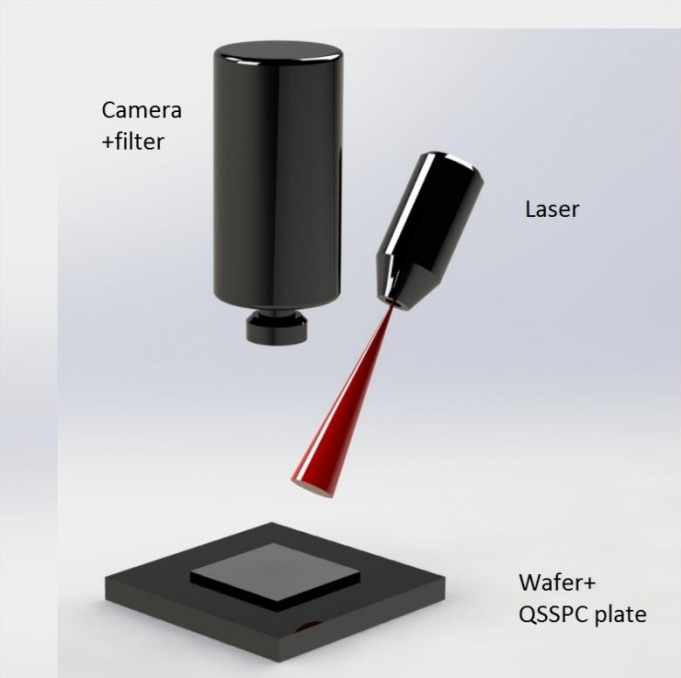


**Figure 5: The PL setup, light from a laser is directed at a wafer positioned on a chuck. Radiative recombination in the wafer causes the emission of photons towards a photo detector camera.**

Laser light of wavelength 808nm is directed at a wafer. A small fraction of the incident and absorbed light is approximately vertically reemitted as a result of radiative recombination from the wafer. A camera is then used to detect what fraction of absorbed incident intensity is reemitted. The laser light itself is stopped from reaching the detector by a filter. The photon

count measured by the photodetector/camera is proportional to the minority carrier density in the wafer/cell.

By performing a QSSPC measurement and a PL measurement of the area above the QSSPC coil, it is possible to relate the intensity reaching the camera to the excess minority carrier density. This ratio is modulated by a constant, hereafter named the calibration constant. It depends upon the optical properties of the sample and must be determined individually for every sample. The calibration constant is subsequently utilized in transferring a larger PL photon count image into an excess minority carrier image. The spatially resolved minority carrier lifetime map is subsequently obtained from equation 2-36.

The major advantage of the PL imaging technique is its ability to provide spatially resolved effective lifetime images quickly (around one second). PL imaging is contactless and immune to trapping effects. One source of inaccuracy stems from photon reabsorption causing an up to 20% error in the minority carrier effective lifetime [19]. However, photon reabsorption can generally be expected to have much less of an impact.

If short illumination times are used, some noise in the obtained data should be expected, as the amount of radiative recombination may not have reached a statistically average value at all pixels in the camera.

By first performing a QSSPC measurement by an induction coil located in the middle of the chuck, one can find the excess minority carrier density at a specific illumination intensity. Performing an uncalibrated PL measurement then allows one to find the correspondence between the excess minority carrier density and the photon count at the detector. This principle is used to find a calibration constant, $C_{Cal}$, used later. The equations used in our setup by bTimaging are confidential and as such not displayed here.

As the above discussion may be a bit too technical to enable easy understanding of how a lifetime map is acquired by PL, a simplified illustration will now be provided. Illumination of a wafer causes an increase in radiative recombination proportional to the excess minority carrier density. The vertically emitted photons reach a detector, allowing for a determination of the excess minority carrier density after performing a QSSPC calibration. The generation rate is known from equation 2-39, allowing the use of equation 2-36 to determine the minority carrier effective lifetime.

# Chapter 3: Experimental details

## Section 3.1: Samples

The samples investigated in the present work were based on industry standard mc-Si wafers produced by Renewable Energy Corporation (REC). The samples include a set of 50 mc-Si wafers from a single block. Due to a large amount of trapping observed in the top of the block, only the first thirty (approximately bottom 58% of the block) are investigated. In addition, the wafers closest to the bottom of the block had a lifetime that was too low to allow for low-illumination QSSPC measurements, causing too much splitting. All wafers were passivated by hydrogenated amorphous silicon in an Oxford PECVD chamber. Relevant wafer parameters are all displayed in table 2.

**Table 2: Parameters of the wafers in the investigated series. Fraction solidified (fs) is the location of the wafer in the block, the bottom of the block having a lower fraction. ρ is the resistivity, and d is the sample thickness.**

| Wafer | fs | ρ[Ω*cm] | d [µm] |
|---|---|---|---|
| 5 | 0.14519 | 1,49 | 165 |
| 6 | 0.16148 | 1.50 | 163.1 |
| 7 | 0.17852 | 1.51 | 163.5 |
| 9 | 0.21333 | 1.51 | 164.3 |
| 10 | 0.23259 | 1.49 | 163.4 |
| 11 | 0.25037 | 1.50 | 163 |
| 12 | 0.26815 | 1.52 | 162.5 |
| 13 | 0.2844 | 1.49 | 164.4 |
| 14 | 0.30222 | 1.46 | 162.8 |
| 15 | 0.31852 | 1.43 | 164.2 |
| 16 | 0.3363 | 1.44 | 163.3 |
| 17 | 0.35259 | 1.44 | 163.5 |
| 18 | 0.37037 | 1.44 | 163.6 |
| 19 | 0.38667 | 1.43 | 163.5 |
| 20 | 0.40444 | 1.42 | 164.8 |
| 26 | 0.50963 | 1.38 | 164 |
| 30 | 0.57778 | 1.33 | 164.4 |

Resistivities were measured using the four-point probe method and averaging over 13 measurement points across the wafer. There exists some uncertainty whether the system in use is accurate (some inconsistencies in measured resistivity), but the measurement results do follow an expected trend. The thickness was inferred from a measurement of the weight. Fraction solidified represents the position of the wafer in the block, where wafer 5 is the closest to the bottom.

## Section 3.2: QSSPC

The QSSPC setup used in this work (Sinton Instruments WCT-120 photo conductance measurement system) is located within the PL equipment, allowing for a QSSPC calibration without moving the wafer. The pulse time was always set to 0.02 seconds in order to ensure steady-state conditions.

## Section 3.3: PL

In this work, the LIS-R1 from bTimaging was used for PL measurements. In order to ensure as little splitting as possible during the first measurement, the illumination was performed using as low as possible intensity values. In addition, short acquisition times were used. This has an effect of "smearing out" the lifetime maps. Grain boundaries become less pronounced, concealing the actual lifetimes. This issue will translate onto Fe images, making it necessary to evaluate the pros and cons of doing so. The most obvious advantage of using low illumination times and intensities is that less splitting occurs during the initial measurement. Another, less obvious advantage, is that the smearing out of the iron concentration allows for an evaluation of the iron content across the wafer where the grain boundaries are hidden, i.e. it becomes easier to evaluate the Fe distribution between grains. It is not unreasonable to think that this may cause the results of both the magnitude and distribution of Fe to be incorrect, but it was found that the iron concentration and distribution obtained still closely followed theoretical expectations and experimental results.

A thorough investigation of the photoconductance calibrated PL imaging technique used in this work was performed by Herlufsen et al.[20].

## Section 3.4: Procedure for Fe mapping

The general procedure developed and used for obtaining raw data for Fe imaging in this work is outlined below.

1) Pretreatment
   a) Perform BO-LID as discussed in section 2.2.2
   b) Allow wafer to relax in dark. Relaxation times were discussed in section 2.2.1
2) First QSSPC measurement
   a) Perform a QSSPC measurement. Use as low an illumination intensity and as short a pulse length as possible. This is discussed in section 4.2.
      i) If trapping is a problem at high excess carrier densities, relocate the wafer and repeat step 2. If sufficiently low illumination levels are used for the QSSPC measurement, it is possible to perform several QSSPC measurements, in order to find an area of low trapping as discussed in section 4.2
3) Initial image; perform a spatially resolved lifetime image acquisition
   a) If external trapping (discussed in section 2.4.3) is only evident at very low excess carrier densities, perform calibration and image acquisition at a $\Delta n$ *below* the crossover point. This ensures minimal splitting during the acquisition of the minority carrier lifetime image.
   b) If external trapping is strongly influencing the QSSPC curve at values close to the crossover point, perform calibration and image acquisition at a $\Delta n$ *above* the crossover point.
4) Second QSSPC image
   a) Perform a new QSSPC measurement, in order to evaluate the amount of FeB splitting that occurred during the first PL measurement. In addition, comparing the obtained QSSPC curves allows for a determination of whether Fe is the dominant recombination center. Review section 2.3.4 for how and why.
5) FeB splitting
   a) Perform several measurements of both QSSPC and lifetime images, instead of performing a single high-intensity illumination step. This must be done in order to avoid degradation of other aspects of the wafer (see section 2.2.2 and section 4.2)
6) Final image
   a) Once the QSSPC curves no longer change from one measurement to the other, almost complete FeB splitting has occurred. Use the first and last images for analysis of the Fe concentration. It is important to perform the last measurement almost immediately after FeB splitting. This is discussed in section 4.3.

This modification of the procedure reported by Macdonald, Tan and Trupke (2008) is transparent and easy to use. It also makes it easy to spot and identify several issues that may influence or even obscure expected results. The next session details some of the problems one may encounter. For reference and visualization, a flow diagram outlining the measurement steps is given in the appendix.

## Section 3.5: Modelling and simulation

The modelling and simulation has been performed using MATLAB. In addition, all figures of experimental results have been imported into MATLAB, which allowed for easy control of axis properties and other visual aspects. Lastly, the transfer of lifetime images into Fe distribution images was also performed using MATLAB.

# Chapter 4: Results

This part of the thesis contains investigations into the validity of the procedure, results of measurements and a discussion of possible error sources. Section 4.1 presents some of the obtained lifetime maps. Section 4.2 discusses effects of illumination during measurement and directly discussed the steps of the proposed procedure for Fe mapping. Section 4.3 investigates the relationship between temperature and association of FeB. Section 4.4 discusses the use of the crossover point for determining whether the lifetime of the sample is dominated by Fe. In section 4.5, Fe maps obtained using the procedure are displayed. Section 4.6 displays results of Fe mapping using a set of wafers from a larger section of the same mc-Si block. In section 4.7 the trends observed are investigated using alternative methods, while section 4.8 relates the observed trends to dislocation clusters.

## Section 4.1: Lifetime maps

This section presents some of the lifetime maps obtained before Feb splitting. A smearing out of the lifetime is evident, which is caused by short acquisition times, as discussed in section 3.3. The lifetimes were measured at an injection density significantly above the crossover point.

The raw data obtained for PL-images included areas outside the wafer position. As such, it was necessary to cut the images. This results in a slight deviation in which parts of a wafer are visible. All samples 13 through 19 were measured at the same position and the images were cut identically. Wafers 7 through 12 were positioned differently and as such, the images have been cut differently. As it was not possible to perform the cutting in any other way than by eye, some difference in both the average lifetime and the average Fe concentration can be expected between the two series.

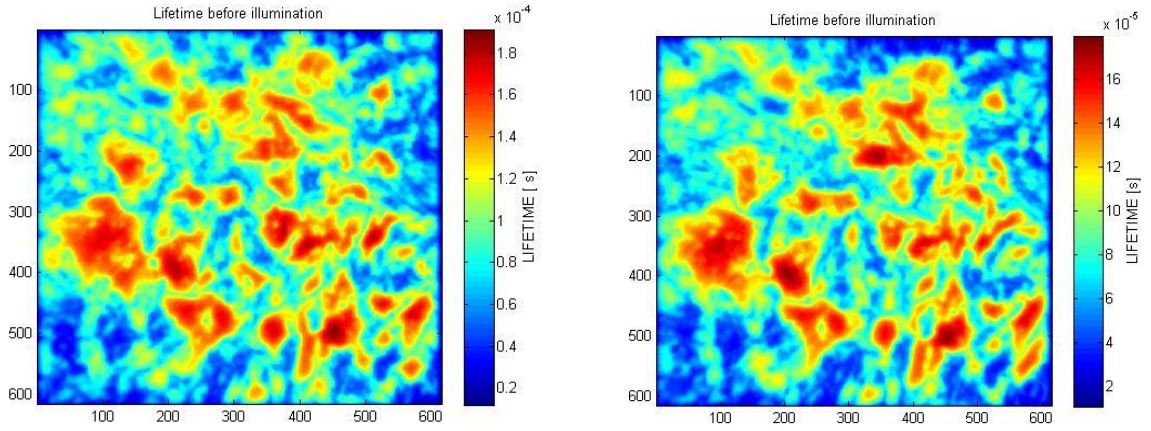


**Figure 6: Lifetime maps obtained for wafers 16 (left) and 17 (right). X and y axes denote pixel location. The colorbars are in units of seconds (difficult to see at this scale, but the values of wafer 16 are multiplied by 1e-4 and wafer 17 by 1e-5).**

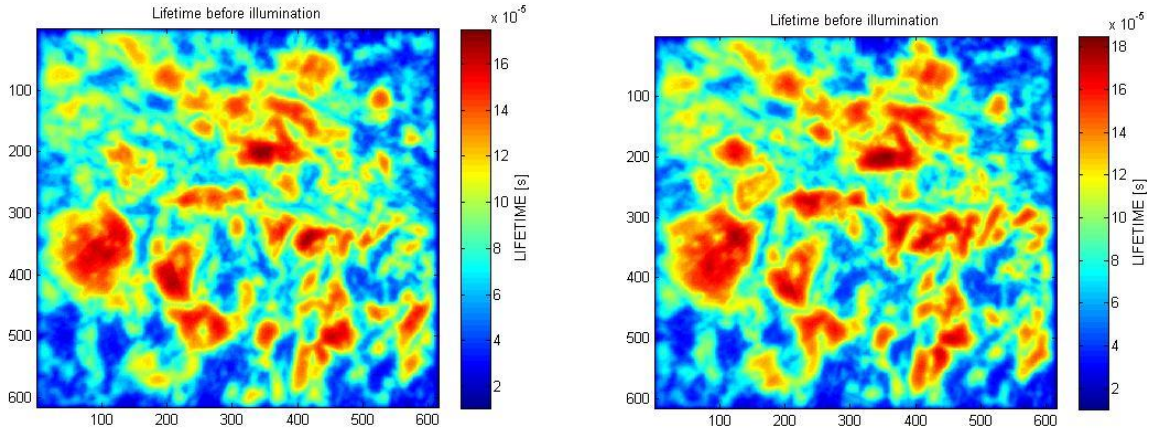


**Figure 7: Lifetime maps obtained for wafers 18(left) and 19(right). X and y axes denote pixel location. Again the colorbars are in units of seconds. The colorbar values are multiplied by 1e-5.**

The figures 6 and 7 depict lifetimes before dissociation of wafers 16 through 19. The axes vary slightly and it is as such of no use to compare magnitudes (an attempt was made, without luck, to correct for this). However, it is still possible to see that the areas of low/high lifetimes stay almost unchanged in going from one wafer to the next. Conventionally, low lifetime is represented by red. The inversion has been performed as it enabled more intuitive comparison to the Fe images.

## Section 4.2: Verification of procedure

This chapter contains a discussion relevant to the Fe mapping procedure, in particular, the effects of illumination during measurements. Where necessary, results of experiments will be included in order to prove certain theories and the validity of certain assumptions. For reference, the discussion will be directly related to the steps of the proposed procedure in section 3.4.

Step 1 (pretreatment) of the procedure has been discussed previously, but for sake of reference will be repeated here. Keeping the wafer in the dark at room temperature for 24 hours ensures almost complete repairing of all FeB complexes (at dopant densities comparable to that of the wafers used in this work). Prior to the relaxation step, it is vital to perform a BO-LID step (see section 2.2.2).

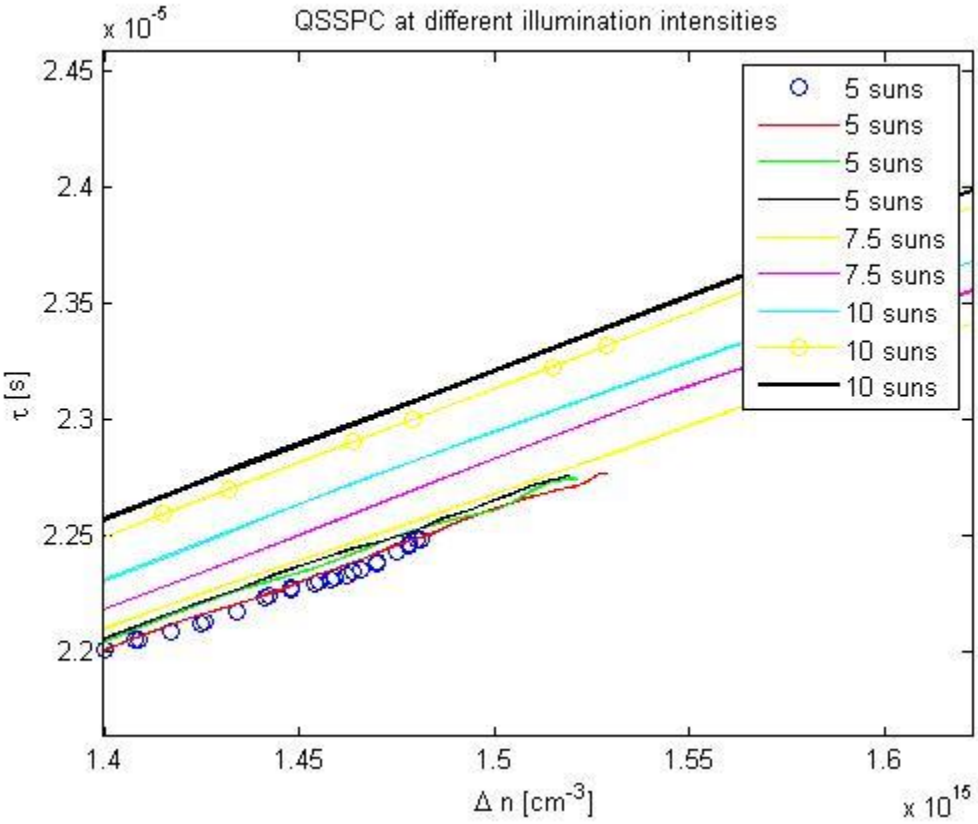


**Figure 8: Zoomed in view of the results obtained by QSSPC measurements on a quasi-mono p-type wafer passivated by amorphous silicon. The values used were determined by trial and error.**

Step 2 (first QSSPC measurement) is based on the results of figure 8. It provides an indication that an illumination level of 5 suns with a pulse length of 0.04 seconds does not cause significant splitting. In contrast, higher illumination intensities cause considerable LID, despite the short illumination time, as indirectly suggested in literature (rate of FeB splitting is proportional to

time but proportional to the illumination intensity squared [21]). The wafer used in this measurement had been allowed to soak in 1 sun for 24 hours prior to being rested in dark for 24 hours. Prior to the last QSSPC measurement (thick black line), the wafer was rested in dark for 4 minutes. This was done in order to avoid a lifetime increase due to an increased wafer temperature. This is to be discussed in section 4.3. Note that for other wafers, an illumination intensity of 5 suns may cause considerable LID, and it may therefore be necessary to use lower illumination intensity in order to avoid splitting. Accumulation of the small amount of splitting during each QSSPC measurement may affect the lifetime image taken later. If this has happened, changes in the QSSPC curves will be evident. If the curves do not change, there still exists some ambiguity. No change (within measurement error) may indicate that no LID has occurred, or that a simultaneous degradation of the passivation layer and FeB splitting has occurred.

During step 2, one must as well evaluate whether or not the lifetime of the wafer is low enough that the measurement is taken under quasi steady state conditions. If the lifetime is high, and the pulse length low, it may be necessary to increase the illumination time in order to ensure steady state conditions.

Even though PL images are not affected by minority carrier trapping, it is still necessary to illuminate the wafer with an intensity that corresponds to an excess carrier density not affected by trapping due to the calibration using QSSPC. It is of interest to use illumination levels corresponding to LLI conditions in order to avoid significant splitting. However, trapping effects may distort the QSSPC curves to such a degree that performing calibration below the crossover point affects the results. Higher injection densities are then, as pointed out in step 3 (initial image), necessary. It is also necessary to avoid calibrating at excess carrier densities too close to the crossover point because the technique becomes less sensitive to Fe [6]. Correcting for trapping may allow for calibration below the crossover point (see section 2.4.3).

After acquiring a PL lifetime image, one should perform a single QSSPC measurement as in step 4. This makes it possible to evaluate the degree of splitting that occurred during the acquisition of the first PL image. This step also enables an evaluation of whether other LID effects have occurred. During the measurements on our wafers it was clear that it is possible to observe changes in the slope of the curve immediately after the first PL measurement.

Step 5 (FeB splitting) was implemented due to an apparent fast degradation of the passivation layer if a single strong, long-exposure step was used. The apparent degradation of the surface layer causes a vertical downshift of the entire lifetime curve. Figure 9 shows the result of QSSPC measurements on a wafer using a long high-intensity illumination step for FeB splitting. A large change in the injection dependent lifetime curve is observed that does not comply with what is to be expected from a dissociation of FeB. Using several long-illumination steps after the last QSSPC measurement resulted in injection dependent lifetime curves almost identical to that of the last measurement, thereby excluding the possibility of incomplete BO-LID. When

performing FeB splitting, using several short illumination steps with a lower intensity, this degradation of the amorphous hydrogenated silicon layer was suppressed.

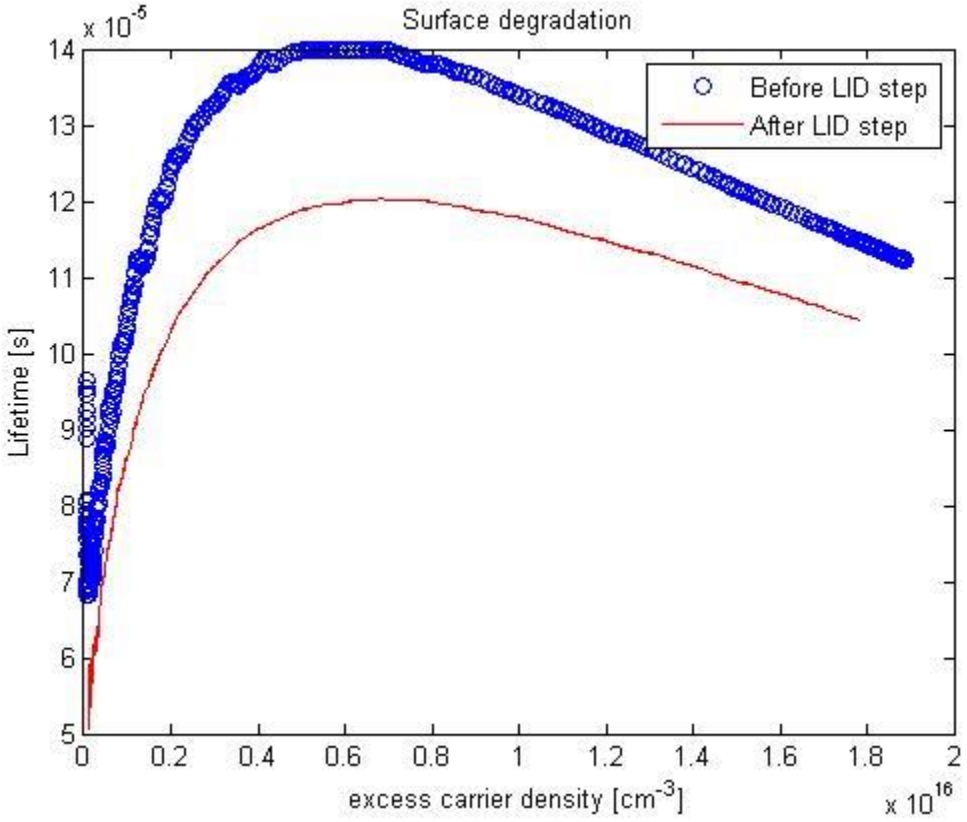


**Figure 9: Observed degradation when using high intensity light.**

Once complete dissociation of FeB has occurred (visible when the QSSPC curves no longer change between measurements) and a final image acquired, the measurement process is complete.

This procedure is more time consuming than the one previously mentioned in literature, erasing some of the advantage of PL imaging. The advantage of using this method, however, is that it enables easy evaluation of sources of error, thus being more transparent and simple to use when testing wafers of less uniformity, such as mc-Si wafers.

Although the suggested procedure is slower than the original, it is still much faster than $\mu W - PCD$. As is shown below, a significant amount of FeB association occurs during the first few minutes after illumination. This causes the last measurement points of the $\mu W - PCD$ to underestimate the Fe concentration significantly

## Section 4.3: Effect of temperature and FeB association

Figure 10 depicts QSSPC measurements obtained on a wafer of the series using the aforementioned procedure. Evident from figure 10, is that some splitting does occur during PL image acquisition. The third curve (green) was taken immediately after the PL-image, showing a significant amount of splitting having occurred.

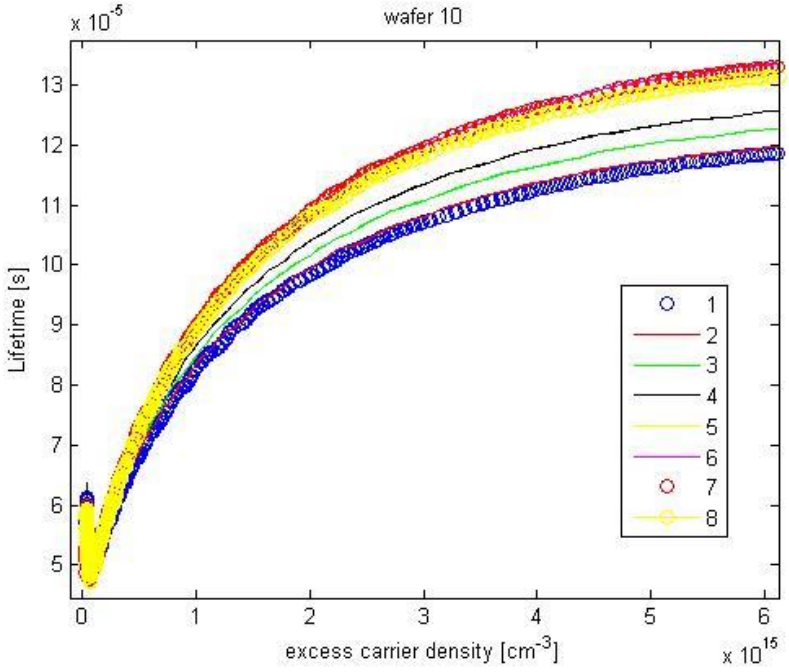


**Figure 10: Several steps of QSSPC and PL image acquisition. Curves 1 and 2 are QSSPC measurements only. Curve 3 was obtained after taking a PL measurement. The wafer was allowed to relax for 3 minutes prior to the last measurement (8).**

It is noteworthy that the last measurement (after a wafer resting time of 3 minutes) shows a decrease in the HLI regime lifetime. This can be expected to occur due to association of FeB pairs. Determining the ideal measurement conditions for obtaining the last image, can be achieved by modelling both the effect of temperature and the effect of FeB association. This is performed in the following.

For a p-type material with a defect energy level well within the lower part of the band gap equation 2-16 for the temperature dependency of the SRH lifetime is reduced to:

$$\tau_{SRH}^{p,maj}(T) = \tau_{n0}(T)\left[\frac{p_0 + p_1(T) + \Delta n}{p_0 + \Delta n} + k\left(\frac{\Delta n}{p_0 + \Delta n}\right)\right] \qquad \text{4-1}$$

while for a p-type material with a defect in the upper part of the band gap it reduces to:

$$\tau_{SRH}^{p,min} = \tau_{n0}(T)\left[1 + k\left(\frac{n_1(T)+\Delta n}{p_0+\Delta n}\right)\right] \qquad \textbf{4-2}$$

Using equations 4-1 and 4-2, the effect of a change in temperature (due to illumination) on the minority carrier lifetime could be investigated. Figures 11 and 12 depict the temperature affected injection dependent lifetime curves that can be expected for interstitial Fe and FeB, respectively. The figures were obtained using the full temperature dependency of equation 2-16. It is clear that a small temperature variation (around 10°C) should not affect the lifetime to a large degree.

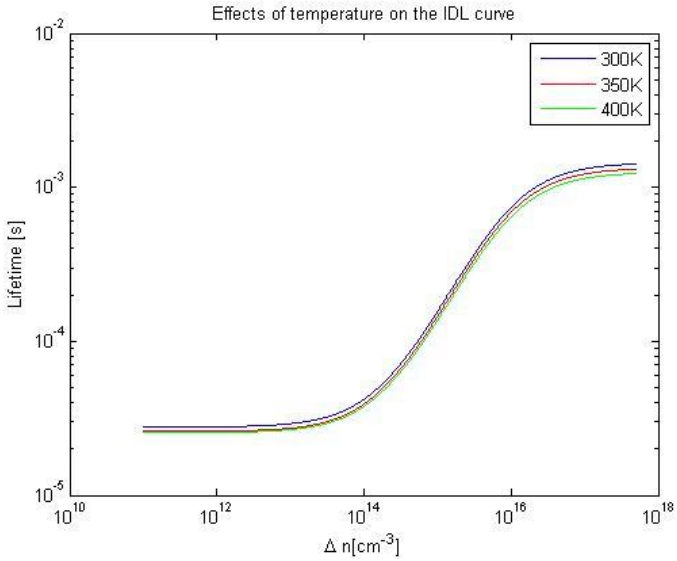


**Figure 11: Injection dependent lifetime curves for different temperatures. A defect concentration of $N_t = 1 * 10^{12}\text{cm}^{-3}$ of Fe and a dopant density of $N_A = 1 * 10^{16}\text{cm}^{-3}$ were used.**

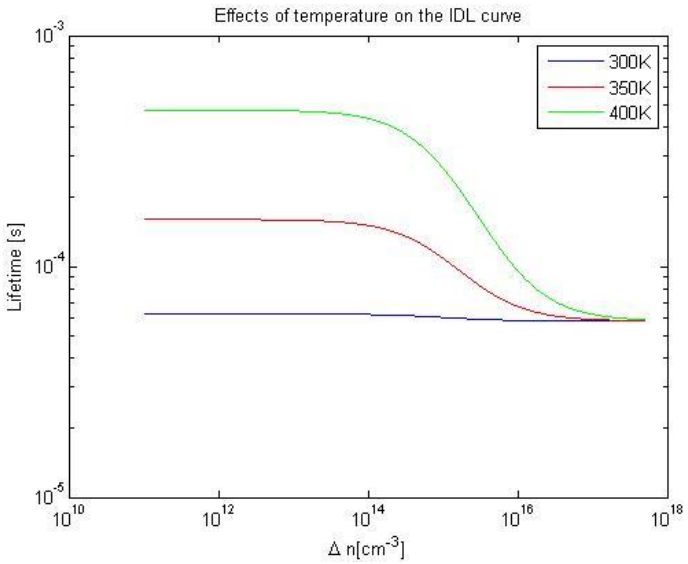


**Figure 12: Temperature dependency of injection dependent lifetime for FeB. A defect concentration of $N_t = 1 * 10^{12}\text{cm}^{-3}$ of Fe and a dopant density of $N_A = 1 * 10^{15}\text{cm}^{-3}$ were used.**

From figure 12 it is clear that a change in temperature affects the SRH-lifetime of FeB across a large excess carrier density range. Both cases were modelled using a defect concentration of 1e12$\text{cm}^{-3}$. All parameters used are those determined by Rein and those measured for the actual wafer. From figure 11, it is apparent that a change in temperature will affect the $Fe_i$ dominated SRH lifetime to some extent. To determine the impact of temperature on the case of figure 10, figure 13 depicts the development of $\tau_{SRH}^{Fe}(T)$ at an excess carrier density of $6.163 * 10^{15}\text{cm}^{-3}$. The interstitial Fe concentration was adjusted to obtain a lifetime similar to that of the measurement. As the lifetime is not singularly decided by the Fe concentration, it results in a slight overestimation of the impact of temperature, but it does give a decent estimation.

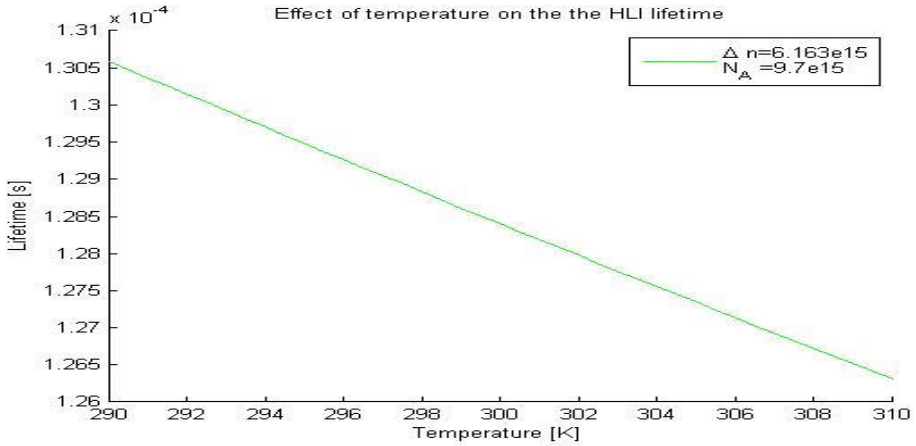


**Figure 13: Effect of a small temperature change on the SRH lifetime, based on actual parameters of the measurement in figure 10. The Fe concentration was set to 1e12 $cm^{-3}$. The HLI lifetime decreases approximately 1% per 7° Kelvin.**

From figure 13 it can be concluded that a decrease in temperature by 4.5 K results in a relative increase of the SRH lifetime by approximately 0.8%. The actual decrease in lifetime between the two last measurements of the measured wafer was approximately 1.5%. For wafer 10, such a small decrease would result in an underestimation of the Fe content of almost 20%. This indicates that the lifetime decrease observed in experiments (consistently) after a short resting period (3 minutes) is due to association of FeB and that FeB association has a much larger effect than a small temperature variation. As such, it is recommended that the last measurement be performed immediately after an FeB splitting step.

## Section 4.4: The crossover point

In section 2.3.3, the theoretical background for utilizing the location of a crossover point as an identifier of Fe presence was discussed. This section covers where one may expect to find the crossover point as a function of the dopant density. In addition, a comparison with experimentally obtained values is provided. Lastly, a discussion of why failing to obtain a crossover point may incorrectly lead to the conclusion that Fe is not the dominant recombination center will be presented.

Table 3 provides an overview of the FeB and Fe defect parameters Rein determined. The maximum and minimum values are based upon the error estimate of the values obtained by Rein. What constitutes a maximum is determined by what value will give the largest crossover point and conversely for the minimum.

**Table 3: Parameters of Rein that have an error estimate. Minimum values correspond to the error estimates that cause the crossover point to lie at the lowest possible excess carrier density.**

| Parameter | Maximum | Intermediate value | Minimum |
|---|---|---|---|
| $k^{Fe}$ | 46 | 51 | 56 |
| $\sigma_n^{Fe}$ | 3.2e-15 $cm^2$ | 3.6e15 $cm^2$ | 4e15 $cm^2$ |
| $E_{FeB}$ | 0.23 eV | 0.26 eV | 0.29 eV |
| $E_{Fe}$ | 0.399 eV | 0.394 eV | 0.389 eV |

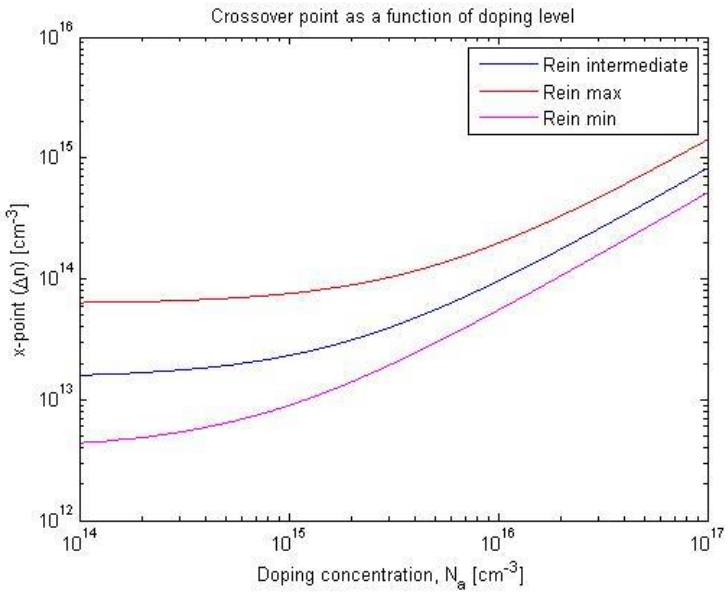


**Figure 14: Crossover point as a function of the doping level.**

Figure 14 was obtained using equation 2-26 with the parameters of table 3. As is immediately apparent, the expectation of the crossover point position varies significantly depending on the chosen parameter constellation. Extending the parameter variation to include those obtained by Macdonald et al [5]. or Istratov et al. [22] would cause an even greater uncertainty. As the parameter variations cause such a large change to the expected crossover point, using a theoretical basis for where to expect a crossover point is fraught with uncertainty.

As the crossover point could be expected to be found below 1e13$cm^{-3}$ for a dopant concentration of 1e15$cm^{-3}$, trapping would in many cases cause the location of the crossover point to be screened. It is therefore recommended that from now on, a change in the slope of the injection dependent lifetime curve along with an increase in HLI lifetime be used as an identifier of Fe instead of the crossover point when examining less than ideal mc-Si wafers (if no crossover point can be located).

The dopant density did not vary enough in the wafer series investigated in this work to be able to compare the obtained crossover point with that expected from theory. Furthermore, the injection dependent lifetime curves were always somewhat influenced by trapping at excess carrier

densities close to the crossover point. The crossover point was (when corrected for trapping) always found somewhere between that expected for Reins maximum values and Reins expected values.

## Section 4.5: Fe concentration through a section of the block

Using the procedure discussed, figures 15 and 16 were obtained. They depict the lifetime of the wafer (before splitting) and the Fe map, respectively. It is immediately apparent that low lifetime areas correspond to high Fe concentration areas, as expected. In addition, a high concentration located at grain boundaries can also be seen.

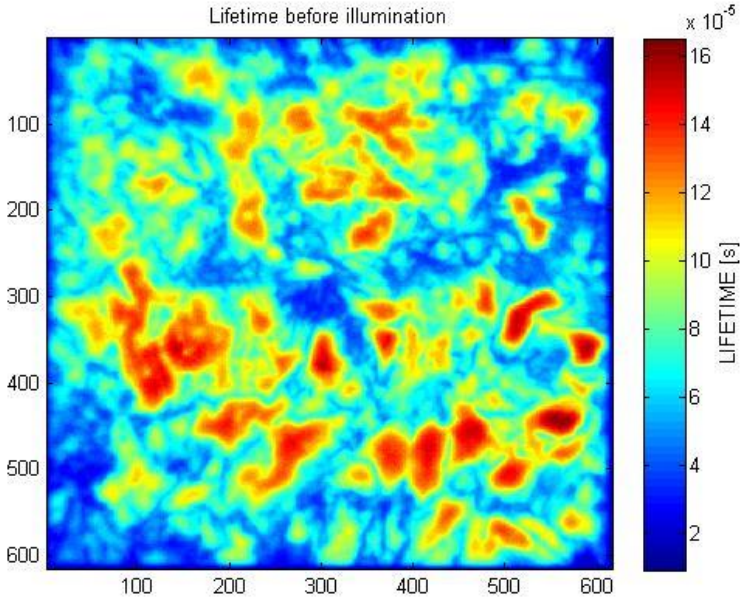


**Figure 15: Lifetime of a wafer as a function of position.**

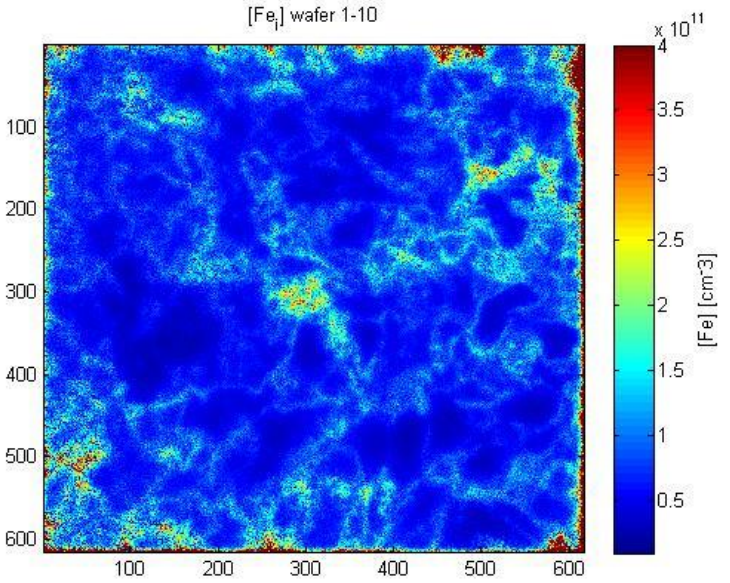


**Figure 16: Iron concentration map. The x and y axes simply depict pixel locations. The high concentration areas correspond well with the low lifetime areas of figure 14 as is to be expected.**

Figure 17 depicts the evolution of the Fe distribution for wafers 7 through 12, while figure 18 presents the Fe concentration for wafers 13 through 19.

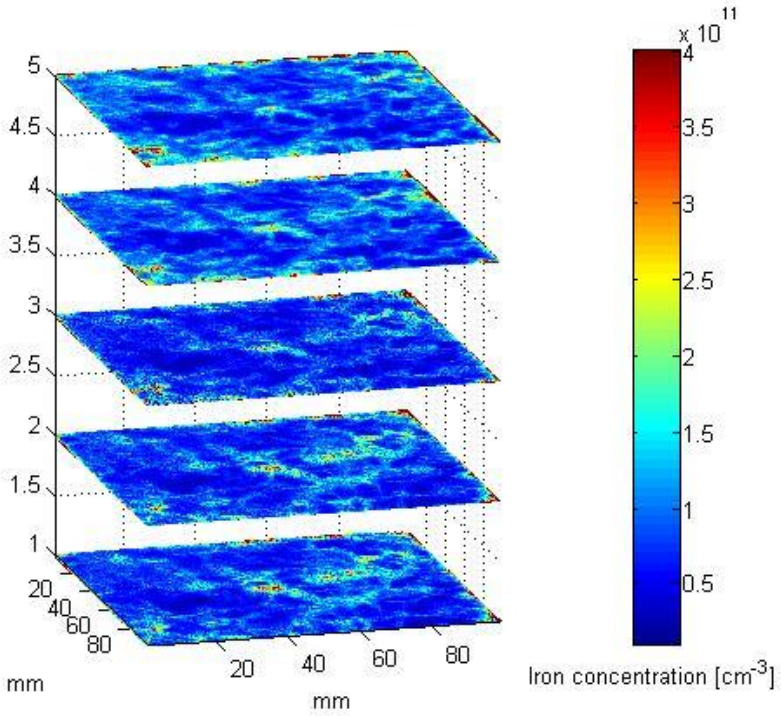


**Figure 17: Fe map of wafers 7 (bottom) to 12 (top), except wafer 8.**

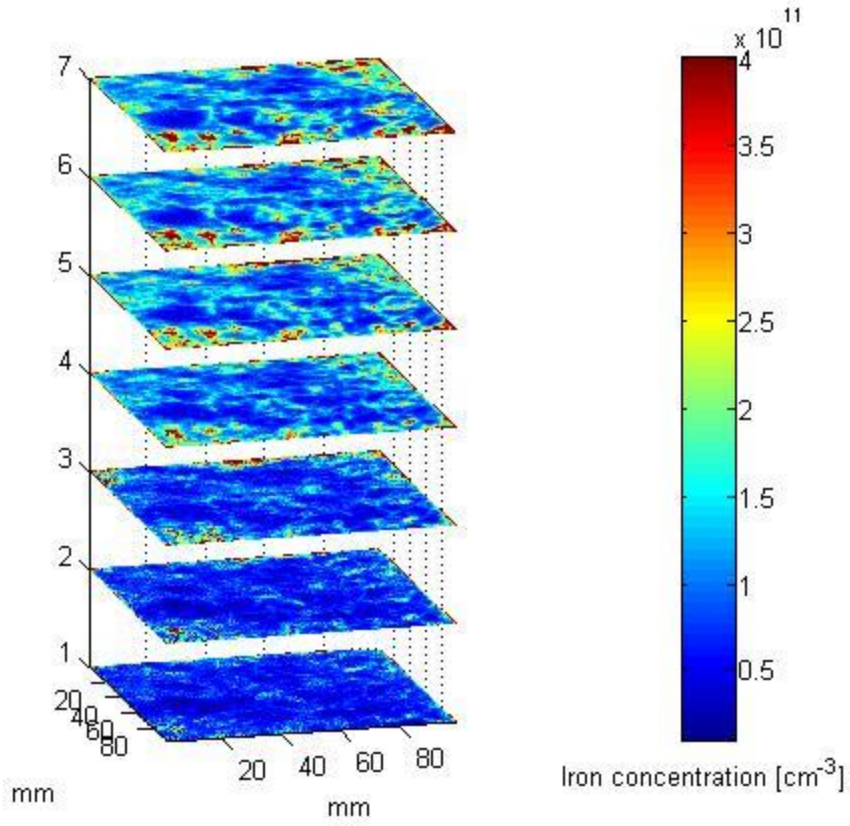


**Figure 18: Fe concentration of wafers 13 (bottom) to wafer 19 (top).**

Scheil's equation [23] is used to predict the lateral distribution of impurities through an ingot. If the partition coefficient is less than 1, an increase in Fe concentration towards the top (last solidified) can be expected. At the bottom of the block a deviation from the Scheil equation values is to be expected due to contamination from the crucible.

Using the Scheil equation and the value of $2*10^{-5}$ for the partition coefficient as found by Kvande et al.[23], it was found that a very small increase in the iron concentration can be expected. They obtained the value of the partition coefficient through a fit of the Fe concentrations obtained in their work. This result is in contrast to what is seen in figures 17 and 18, where the average increase in Fe concentration when going towards the top of the block is larger than what can be suspected from a fit to the Scheil equation. Table 4 shows the average Fe concentration of the wafers in figure 18.

**Table 4: Average Fe concentration for the wafers in figure 17**

| Wafer | 13 | 14 | 15 | 16 | 17 | 18 | 19 |
|---|---|---|---|---|---|---|---|
| $[Fe_i]_{av}\ cm^{-3}$ | 7.8e10 | 8.8e10 | 1.07e11 | 1.25e11 | 1.48e11 | 1.56e11 | 1.60e11 |

In figure 18 there is a clear tendency of the poor regions of the wafer becoming worse more rapidly than the good regions. It is possible that these areas contain a high amount of other defects, changing the segregation coefficient for Fe between melt and solid. Fe has been thought to segregate into extrinsic defects in the solid phase, thereby increasing the total Fe concentration above what could otherwise be assumed, as reported by Kvande et al. Their work indicated that such a mechanism was suppressed. The results of table 4, figure 17 and figure 18 in the present work indicate that such a mechanism is present and is indeed the cause of a rapid increase in Fe concentration towards the top of the block.

### Section 4.6: A second look at Fe concentrations

Figure 19 depicts the PL images of wafers 10, 15, 20, 26, and 30, while table 5 shows the average Fe content. The lifetime images used to obtain the Fe concentration maps were acquired using a PL acquisition time of 0.8s to ensure sharp images. The same trend as was found earlier is seen here; the Fe concentration is found to increase rapidly when moving from about 23% above the bottom of the block to about 58% above it. That it is the increase in the Fe concentration of the high-concentration areas that are responsible for this rapid increase is not as clear as in figures 17 and 18. Conversely, it is quite clear that the areas of low concentration stay, for the most part, depleted of Fe.

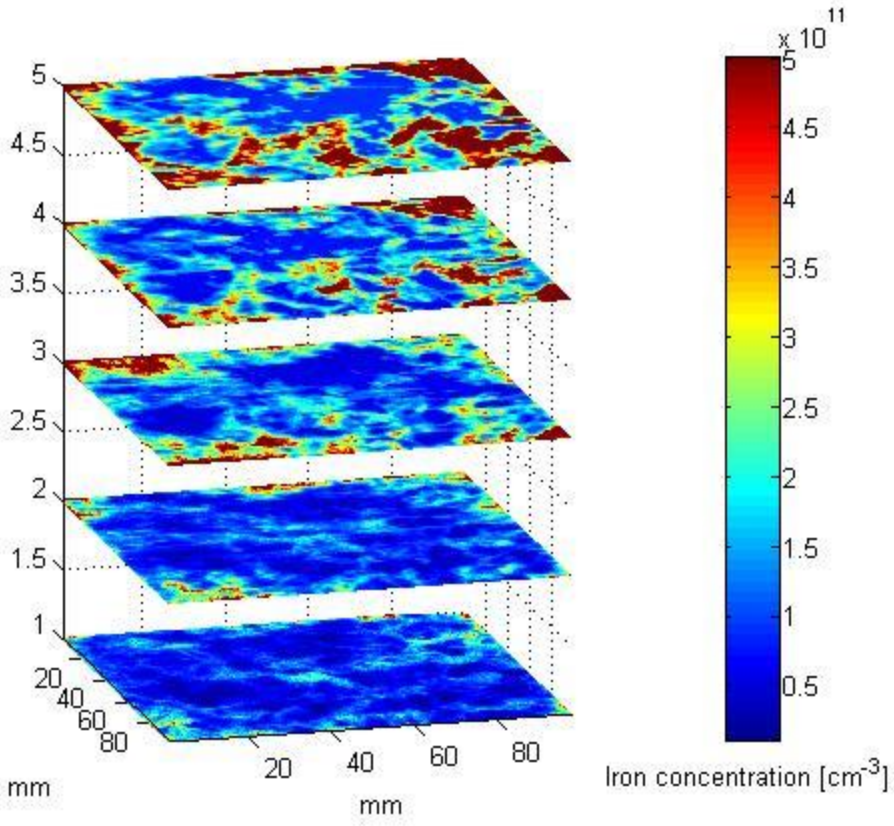


**Figure 19: From bottom to top: Wafer 10, 15, 20, 26, and 30**

**Table 5: Average Fe concentrations as obtained from the PL images**

| Wafer | 10 | 15 | 20 | 26 | 30 |
|---|---|---|---|---|---|
| $[Fe_i]_{av}\ cm^{-3}$ | 9.48e10 | 1.15e11 | 1.82e11 | 2.25e11 | 3.19e11 |

## Section 4.7: Fe concentration trends determined by alternative means

### Section 4.7.1: Fe concentrations obtained by QSSPC

While the magnitude of Fe concentration obtained from the PL and the QSSPC are not expected to be equal due to the difference in measured area (QSSPC measures only a small area around a coil located in the middle of the setup), it is of interest to compare the magnitudes, as the first QSSPC is taken before any FeB splitting has occurred. Figure 20 depicts the change in Fe concentration for the wafers of figure 18.

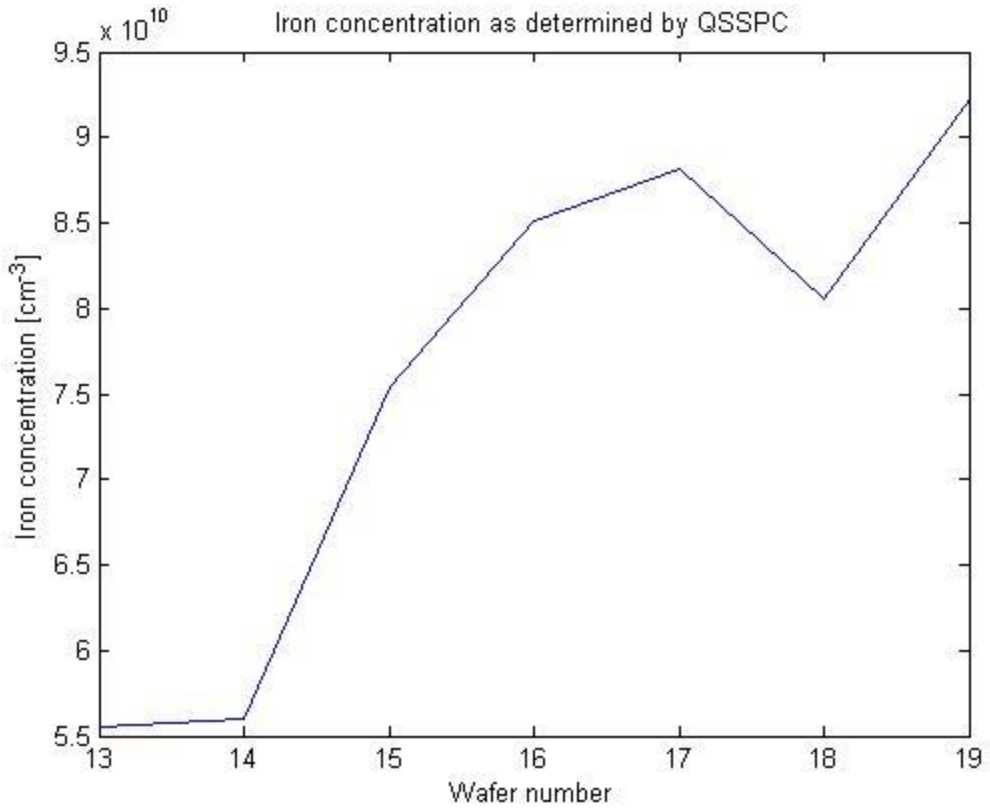


**Figure 20: Average Fe concentration as determined by QSSPC for wafers 13 through 19.**

The change in magnitude determined by QSSPC is slightly lower than what was determined from PL, but still of a comparable size. The slightly lower Fe concentration may be due to the area measured actually having a lower Fe concentration (the QSSPC coil measured a small area approximately in the center of the wafers). The close match between QSSPC and PL gives a lot of confidence in the results of the spatially resolved Fe images.

### Section 4.7.2: Change in area fraction of high Fe concentration

By investigating the Fe distribution of the wafers using histograms, it was revealed that the change in average Fe concentration was due to a general increase across all areas of the wafer, but in particular, a large increase in the very high (much higher than the average Fe concentration) concentration areas.

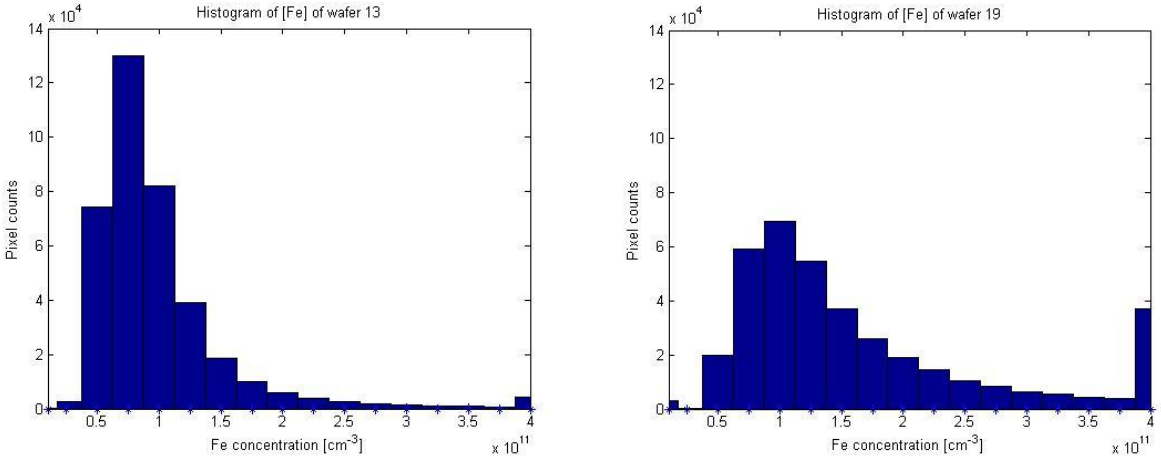


**Figure 21: Histograms of the Fe concentration on wafer 13 (left) and wafer 19 (right). As can be seen, the amount of pixels containing a very high concentration of Fe increases substantially.**

Figure 21 depicts histograms relating Fe concentration and pixel count for wafers 13 and 19. It is apparent that the amount of very high concentration areas (more than 4e11 $cm^{-3}$) increases substantially when going towards higher wafer numbers.

## Section 4.8: Fe trends and dislocation clusters

All wafers of the series used in this work were previously investigated by R. Søndenå et al.[24]. They obtained lifetime images of all wafers through the series and created a map of a cross-section of the block. Figures 22 and 23 display the results. Images were obtained with permission from R. Søndenå.

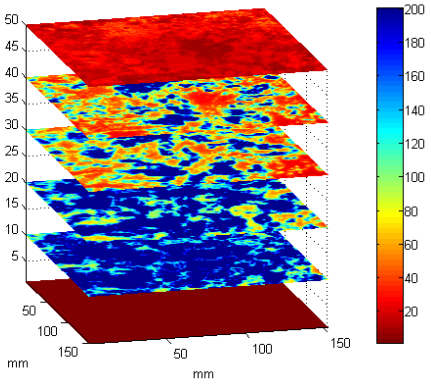


**Figure 22: Lifetime through the block investigated in this work. The figure was obtained from ref 24, with permission from Rune Søndenå.**

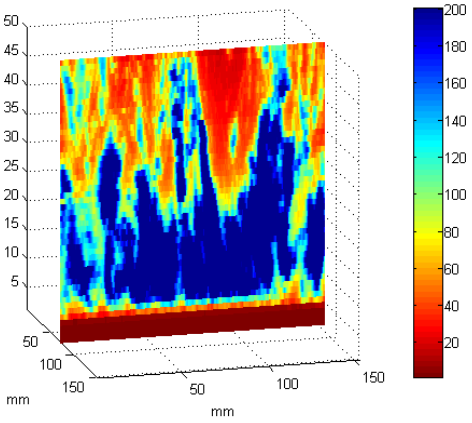


**Figure 23: Crosssection of the lifetime through the block investigated in this work. The figure was obtained from ref 24, with permission from Rune Søndenå.**

Note that the wafers used in this work were cut 5 centimeters from the edge of those used in figures 22 and 23. They explained the low lifetime towards the top of the block by an increase in dislocation clusters. This increase in dislocation clusters matches the areas of high Fe concentration found in this work, indicating that the rapid increase in Fe concentration is due to an increase in dislocation clusters.

# Chapter 5: Discussion

## Section 5.1: Sources of error

Sources of error that may have influenced the results obtained in this work include splitting during PL-imaging, uncertainties in the resistivity measurements, and some uncertainty regarding the completeness of BO-LID. The amount of splitting during PL-imaging could not be reduced as trapping made low-level injection measurements difficult. It is conceivable that the prefactor (of equation 2-29) being excess carrier density dependent can influence the spatial variation of Fe concentration. It was in the discussion of Fe concentration trends assumed that this did not influence the results. The uncertainty in the resistivity measurements was discussed previously. Assuming a 20% underestimation in the derived doping density, the Fe concentration is underestimated by 10% for the specific case of wafer 10. An underestimation of the resistivity also affects the lifetime measurements themselves, although this effect is expected to have a lesser impact, particularly for measurements performed at high excess carrier densities.

There was a slight drop in the obtained Fe concentration in going from set 1 (wafers 7 through 12) to set 2 (wafers 13 through 19). As the two sets had been illuminated for different times regarding BO-LID, it is possible that the results of these measurements were influenced by an incomplete BO-LID. However, these wafers were illuminated for a long time, which should ensure that minimal BO-LID could occur during our measurements. Additionally, the short illumination time during FeB splitting would, in theory, cause an insignificant amount of BO-LID (the FeB splitting saturated after an accumulated 5 seconds of 1 sun illumination on all wafers 7 through 19). In order to exclude any possible influence of BO-LID, a third batch of wafers (section 4.6) were illuminated for 96 hours, using a much higher illumination intensity (the exact illumination intensity is unknown, but it was a minimum of 10 times higher than what was previously used). The Fe concentration magnitudes and trends of the first measurements were still seen for the wafers used in the second look at Fe concentrations, indicating that the impact of BO-LID upon the first Fe concentration measurements was small.

In all measurements a few pixels returned negative values of Fe concentration. This is caused by a large variation of the excess minority carrier density over the wafer, or equivalently, a large variation in the lifetime. This causes the low-lifetime areas to lie beneath the crossover point. Alternatively, this may have simply been measurement artifacts. Radiative recombination is small in Si, and the detection of this small amount is difficult and for short PL acquisition times, not large enough to reach a statistical average (i.e.. some pixels might detect more photons during a second measurement using the same measurement conditions).

Other sources of (smaller) uncertainties are listed below:

1. The QSSPC excess carrier density dependent lifetime is affected by trapping over a large range, causing the lifetime to be overestimated, even at excess carrier densities above the crossover point.
2. The calibration of PL by QSSPC. The calibration process assumes complete uniformity of the optical properties across the wafer.
3. While the degradation of the surface passivation layer was no longer observable when using the new procedure, some small undetectable amount may still have influenced the results by decreasing the lifetime after FeB splitting.

## Section 5.2: Validity of procedure

The combined effect of the many sources of error leads to a rather large uncertainty in the magnitude of the Fe concentration in addition to a smaller uncertainty in the distribution. On the other hand, the Fe concentrations obtained for the wafers in this work are within an order of magnitude expected for them. In addition, areas of high concentration correspond to areas of low lifetime, indicating that the calculated spatial distribution pattern of Fe is correct.

The discrepancy between the average Fe concentration evolution vertically through the block obtained in this work and that of Kvande et al. and Macdonald [25] may be indicative of an inaccuracy in the measurements of this work. However, the wafers for which the BO-LID uncertainty had unequivocally been eliminated (decreasing the uncertainty in the measurements considerably) showed the same development. In addition, the close match between the dislocation cluster increase and the increase in high Fe content areas suggest that the distribution and change in Fe concentration magnitude are accurate.

The amount of splitting that occurs during the first PL image acquisition and its exact impact on the Fe concentration has not been quantified in this work. It is reasonable to assume that the results are affected by this splitting due to the lifetime increase (as seen in figure 10) after the first PL imaging. However, as the splitting occurs *during* the measurement, a large proportion of the measurement is virtually splitting-free.

## Section 5.3: Possible improvements upon the procedure or the measurements specific to this work

Schubert, Habenicht, and Warta [26] recently reported an enhancement to the calculation of Fe concentration. They provided a suggestion for an improved prefactor (equation 2-29) that accounts for incomplete association/dissociation of FeB. This method requires knowledge of the extent of splitting that occurs during the first measurement.

As incomplete BO-LID may have influenced some of the measurements, improving upon the BO-LID procedure used in this work would increase the accuracy and eliminate some of the uncertainties.

The uncertainty in the accuracy of the resistivity measurement could have been eliminated by the acquisition of new equipment. Time did not allow for this adjustment during this research.

A quantification of the ideal excess carrier density to perform a PL measurement could decrease the amount of splitting that occurs during the acquisition of the first image.

By use of established methods for correction of minority carrier trapping, it would be possible to extend the range of wafers that could be tested. In addition, it could have allowed for measurements below the crossover point, ensuring minimal splitting during acquisition of the first PL measurement.

# Chapter 6: Conclusions

In this work, a procedure for using PL-imaging for Fe concentration mapping was developed. This procedure allowed for a great reduction of effects such as FeB association, surface layer degradation, and temperature during the measurement of the Fe concentration. The goal of enabling easy evaluation of results was achieved by developing a procedure that allowed for analysis during the measurement process. This was done by introducing several new steps in the procedure.

Estimations regarding the accuracy of the procedure were provided. It was found that some of the results contained rather large uncertainties. Conversely, the Fe concentrations obtained seemed reasonable and were within an order of magnitude of what were expected for these wafers. Due to it being difficult to quantify some of the largest sources of error, a quantification of the total uncertainty cannot be provided. However, a qualified guess would be that the Fe concentrations obtained using the procedure of this work lie within an order of magnitude of the actual concentration. In addition, it is reasonable to assume that the Fe concentration is underestimated rather than overestimated.

As was suggested in section 1.2: “Purpose of this work”, investigating trends in Fe distribution through a block enabled an identification of the likely cause of high Fe content. It was found in this work that Fe tends to segregate into dislocation clusters during crystal growth. Thus enabling higher concentrations of Fe than what would otherwise be expected. This result reveals why production methods that decrease the dislocation cluster density have the added benefit of decreasing the amount of Fe in the finished product.

## Further work

1. Implementation of the suggestions for improvement upon the procedure discussed in section 5.3 and a subsequent evaluation of the smaller uncertainties that would then be expected to be the largest could improve the accuracy of the technique and decrease the uncertainty of results considerably.
2. Investigation of a wafer set with a larger dopant density range would enable an extension to the work concerning the crossover point. It may be possible to narrow the range of parameters such as the capture cross-sections and defect energy levels of interstitial Fe and FeB.

# References


[1] Bazilian M., Onyeji I., Liebreich M., MacGill I., Chase J., Shah J. , and Zhengrong S. (2013). Re-considering the economics of photovoltaic power. *Renewable Energy*, *53*, 329-338.

[2] Masson, G. (iCARES Consulting), Orlandi S., Rekinger M., (2014). Global market outlook for photovoltaics 2014-2018. Retrieved from http://www.epia.org/news/publications/

[3] Zoth, G. and Bergholz, W. (1990). A fast, preparation-free method to detect iron in silicon, *J. Appl. Phys.* Vol.67, 6764

[4] Macdonald D., Tan, J. , and Trupke, T. (2008). Imaging interstitial iron concentrations in boron-doped crystalline silicon using photoluminescence, *J. Appl. Phys* 103, 073710

[5] Macdonald, D. , Roth, T. , and Deenapanray, P.N. (2006). Doping dependence of the carrier lifetime crossover point upon dissociation of iron-boron pairs in crystalline silicone, *Applied Physics Letters*, 89, 142107

[6] Macdonald, D.H. , Geerligs, L.J. , and Azzizi, A. (2004). Iron detection in crystalline silicon by carrier lifetime measurements for arbitrary injection and doping, *J. Appl. Phys*, 95, 1021

[7] Nærland, T.U., Angelskår, H. , Kirkengen, M., Søndenå, R. , and Marstein, E. S. (2012). The role of excess minority carriers in light induced degradation examined by photoluminescence imaging, *J.Appl.Phys*. 112, 033703

[8] Bothe, K. , Sinton, R. ,and Schmidt, J. (2005). Fundamental boron-oxygen-related carrier lifetime limit in mono- and multicrystalline silicon. *Prog. Photovolt: Res. Appl*.; 13:287–296

[9] Naerland, T.U., Angelskår, H., and Marstein, E.S. (2013). Direct monitoring of minority carrier density during light induced degradation in Czochralski silicon by photoluminescence imaging, *J. Appl. Phys*. 113, 193707

[10] Savin, H., Yli-Koski, M., & Haarahiltunen, A. (2009). Role of copper in light induced minority-carrier lifetime degradation of silicon. *Applied Physics Letters*, *95*(15), 152111.

[11] Rein, S. (2005). *Lifetime Spectroscopy, A Method of Defect Characterization in Silicon for Photovoltaic Applications.* Germany: Springer-Verlag Berlin Heidelberg.

[12] Green, M.A. (1990). Intrinsic concentration, effective densities of states, and effective mass in silicon. *J. Appl. Phys*, 67, 2944

[13] Kerr, M.J., and Cuevas, A. (2002). General parameterization of Auger recombination in crystalline silicon, *J. Appl. Phys*, 91, 2473

[14] Yakimov, E. B. (2005). EBIC and DLTS characterization of pure Si crystals. *Bulletin of Materials Science*, *28*(4), 367-371.

[15] Lagowski, J., Edelman, P., Dexter, M., & Henley, W. (1992). Non-contact mapping of heavy metal contamination for silicon IC fabrication. *Semiconductor Science and Technology*, *7*(1A), A185.

[16] Lauer, K., Laades, A., Übensee, H., Metzner, H., & Lawerenz, A. (2008). Detailed analysis of the microwave-detected photoconductance decay in crystalline silicon. *Journal of Applied Physics*, *104*(10), 104503.

[17] Sinton, R. A., Cuevas, A., & Stuckings, M. (1996, May). Quasi-steady-state photoconductance, a new method for solar cell material and device characterization. In *Photovoltaic Specialists Conference, 1996., Conference Record of the Twenty Fifth IEEE* (pp. 457-460). IEEE.

[18] Macdonald, D., Sinton, R.A , Cuevas A. (2001) On the use of a bias-light correction for trapping effects in photoconductance-based lifetime measurements of silicon, J. *Appl. Phys*, 89, 2772

[19] Trupke, T. (2006). Influence of photon reabsorption on quasi-steady-state photoluminescence measurements on crystalline silicon, *J. Appl. Phys*, 100, 063531

[20] Herlufsen, S., Schmidt, J., Hinken, D., Bothe, K., & Brendel, R. (2008). Photoconductance-calibrated photoluminescence lifetime imaging of crystalline silicon. *physica status solidi (RRL)-Rapid Research Letters*, *2*(6), 245-247.

[21] Geerlings L. J., and Macdonald, D. (2004). Dynamics of light-induced FeB pair dissociation in crystalline silicon. *Appl. Phys. Letters*, 85, 5227

[22] Istratov, A. A., Hieslmair, H., & Weber, E. R. (2000). Iron contamination in silicon technology. *Applied Physics A*, 70(5), 489-534.

[23] Kvande, R., Geerlings, L.J., Coletti, G., Arnberg, L., Di Sabatino, M., Øvrelid, E.J., and Swanson, C.C. (2008). Distribution of iron in multicrystalline silicon blocks, *J. Appl. Phys*, 104, 064905

[24] R. Søndenå, J. Gjessing, H. Angelskår, Ø. Nordseth, S.E. Foss, and E. S. Marstein, Effects of dislocations on the electrical response of multicrystalline silicon solar cells, 28th European Photovoltaic Solar Energy Conference and Exhibition.

[25] Macdonald, D., Cuevas, A., Kinomura, A., Nakano, Y., Geerligs, L. J.(2005). Transition-metal profiles in a multicrystalline silicon ingot, *J. Appl. Phys.*97, 033523.

[26] Schubert, M. C., Habenicht, H., & Warta, W. (2011). Imaging of metastable defects in silicon. *Photovoltaics, IEEE Journal of*, *1*(2), 168-173.

# Appendix

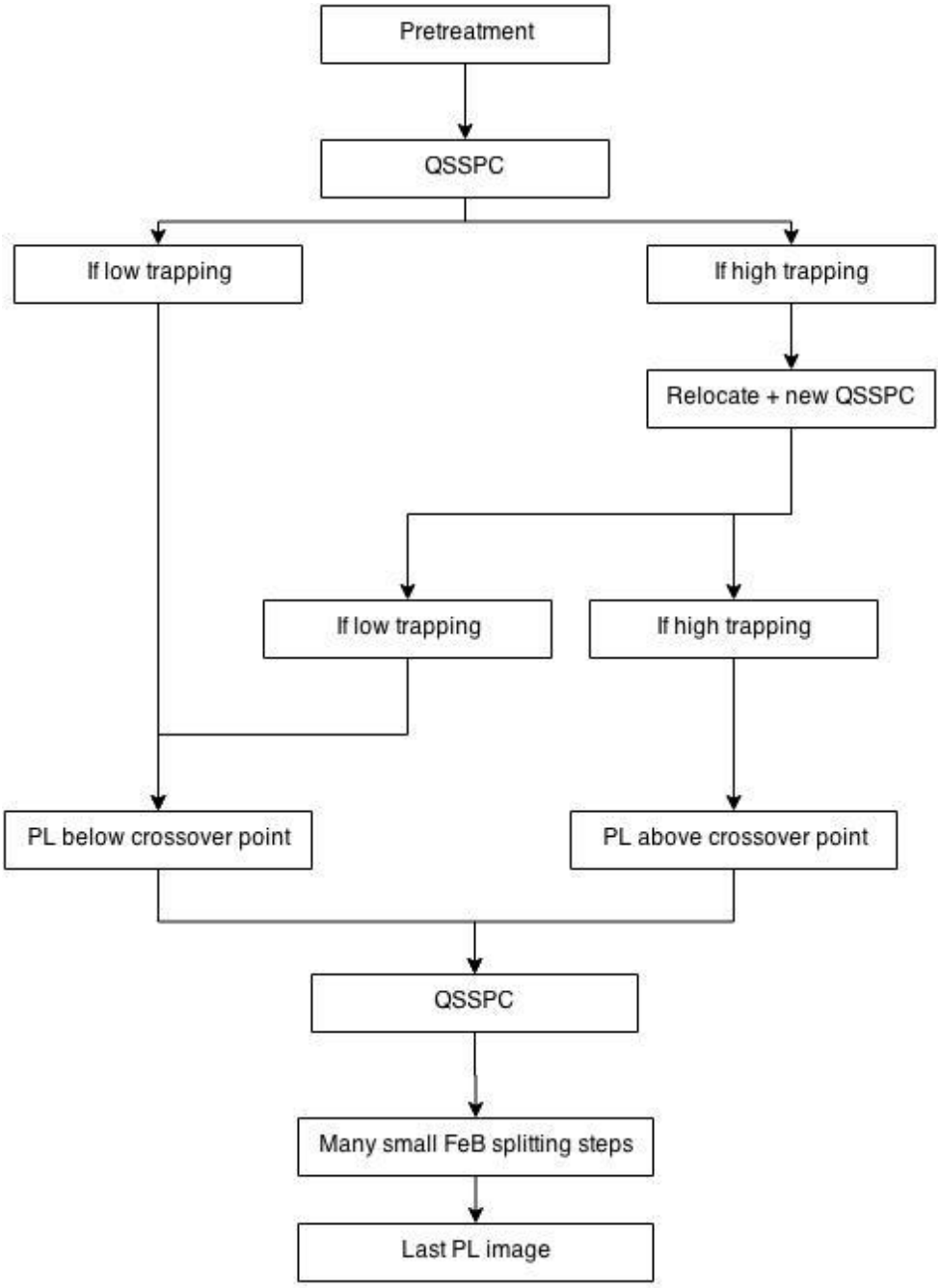
Pretreatment
QSSPC
If low trapping
If high trapping
Relocate + new QSSPC
If low trapping
If high trapping
PL below crossover point
PL above crossover point
QSSPC
Many small FeB splitting steps
Last PL image